



Polyphase stratabound scheelite-ferberite mineralization at Mallnock, Eastern Alps, Austria

Florian Altenberger¹ · Joachim Krause² · Niki E. Wintzer³ · Christoph Iglseder⁴ · Jasper Berndt⁵ · Kai Bachmann² · Johann G. Raith¹

Received: 10 July 2023 / Accepted: 31 January 2024
© The Author(s) 2024

Abstract

A peculiar type of stratabound tungsten mineralization in metacarbonate rocks was discovered and explored at Mallnock (Austria) during the late 1980s. It is the only tungsten occurrence in the Eastern Alps in which scheelite is associated with wolframite (96 mol% ferberite). The tungsten prospect is located in the Austroalpine Drauzug-Gurktal Nappe System recording polyphase low-grade regional metamorphism. Raman spectroscopy of carbonaceous material yield maximum metamorphic temperatures of 296 ± 27 °C and 258 ± 27 °C, which are assigned to Variscan and Eoalpine metamorphism, respectively. Scheelite and ferberite occur as polyphase stockwork-like mineralization in Fe-rich magnesite in the northern ore zone (Mallnock North), whereas in the western ore zone (Mallnock West), scheelite-quartz veinlets are exclusively hosted in dolomitic marbles. LA-ICP-MS analyses of scheelite and ferberite yield low contents of Mo, Nb, Ta, and rare earth elements, but high contents of Na and Sr. Uranium is particularly high in scheelite (up to 200 µg/g) and makes this mineral a suitable target for U–Pb dating. In situ U–Pb dating of scheelite yielded an early Permian age (294 ± 8 Ma) for Mallnock West and a Middle Triassic age (239 ± 3 Ma) for Mallnock North. A monzodioritic dike close to Mallnock yielded a U–Pb apatite date of 282 ± 9 Ma and supports the polyphase formation of this mineralization. The U–Pb scheelite ages indicate that a model for tungsten metallogeny in the Eastern Alps must also consider remobilization of tungsten by metamorphic fluids. In the Alps, the Permian to Triassic period (ca. 290–225 Ma) is characterized by an overall extensional geodynamic setting related to the breakup of Pangea. Lithospheric thinning caused higher heat flow, low-P metamorphism, and anatexis in the lower crust, which led to enhanced crustal fluid flow in the upper crust. These processes were not only responsible for the formation of metasomatic hydrothermal magnesite and siderite deposits in the Eastern Alps but also for this unique magnesite-ferberite-scheelite mineralization at Mallnock.

Keywords Scheelite · Wolframite · LA-ICP-MS trace element analyses · Raman spectroscopy · U–Pb dating · Eastern Alps

Editorial handling: M. Harlaux

✉ Florian Altenberger
florian.altenberger@unileoben.ac.at

- ¹ Montanuniversität Leoben, Department Applied Geosciences and Geophysics, Chair of Resource Mineralogy, Peter Tunner-Straße 5, 8700 Leoben, Austria
- ² Helmholtz-Zentrum Dresden-Rossendorf, Helmholtz Institute Freiberg for Resource Technology, Chemnitz Straße 40, 09599 Freiberg, Germany
- ³ U.S. Geological Survey, 904 W. Riverside Ave, Spokane, WA 99201, USA
- ⁴ GeoSphere Austria, Hohe Warte 38, 1190 Vienna, Austria
- ⁵ Westfälische Wilhelms-Universität Münster, Institute for Mineralogy, Corrensstraße 24, 48149 Münster, Germany

Introduction

Exploration for tungsten by VOEST Alpine AG during the late 1980s in Austria led to the discovery of a peculiar type of tungsten mineralization at Mallnock (Neinavaie 1984). The unique feature that sets Mallnock apart from other tungsten deposits in the Eastern Alps is the association of scheelite with ferberite. This stratabound tungsten mineralization is hosted in low-grade metacarbonate rocks (Fe-bearing dolomite and magnesite) without any apparent link to magmatic intrusions (Neinavaie et al. 1989). Although scheelite occurs in many localities throughout Europe, wolframite is commonly restricted to granite-related vein-type and greisen deposits (e.g., in the European Variscides, Webster et al. 2004; Simons et al. 2017; Harlaux et al.

2018a; Michaud et al. 2020; Launay et al. 2021). However, in the Alpine orogen, wolframite is extremely rare (Feitzinger et al. 1995; Ferenc and Uher 2007).

The tungstates, scheelite (CaWO_4) and wolframite ($[\text{Fe},\text{Mn}]\text{WO}_4$), can incorporate various trace elements into their crystal structure (e.g., Hazen et al. 1985; Macavei and Schulz 1993). Laser ablation-inductively coupled plasma-mass spectrometry (LA-ICP-MS) allows in situ analysis of minor and trace elements in scheelite and wolframite as well as radiometric dating (Harlaux et al. 2018b; Yang et al. 2020; Carr et al. 2021). Both minerals have been used to constrain the physicochemical conditions and chemistry of ore-bearing fluids and to constrain the genesis of tungsten deposits. Most of these studies focused mainly on scheelite (e.g., Poitrenaud et al. 2020; Roy-Garand et al. 2022; Wintzer et al. 2022) or on wolframite (e.g., Harlaux et al. 2018a; Chen et al. 2020; Xie et al. 2022) and only a few combined both minerals (e.g., Zhang et al. 2018; Li et al. 2022).

Scheelite is most common in Ca-rich lithologies, particularly in skarn deposits. Most skarn deposits show a spatial connection and genetic relationship to nearby fractionated granitic intrusions, which are interpreted as the source of magmatic-hydrothermal tungsten mineralization (e.g., King Island, Australia, Kwak and Tan 1981; Cantung and Mactung, Canada, Roy-Garand et al. 2022). Likewise, wolframite-rich vein and greisen deposits are commonly linked to high-temperature magmatic-hydrothermal fluids related to intrusions in Ca-poor, silica-saturated systems (e.g., Zinnwald, Erzgebirge, Germany/Czech Republic, Webster et al. 2004; Panasqueira, Portugal, Lecumberri-Sanchez et al. 2017; Massif Central, France, Harlaux et al. 2018b; Hunan Province, China, Li et al. 2022). Moreover, metamorphogenic models were proposed exclusively for tungsten deposits in other geological settings (e.g., Pilok, Thailand, Linnen and Williams-Jones 1995; Nova Scotia, Canada, Dostal et al. 2009; Otago Schist, New Zealand, Cave et al. 2017; Palmer et al. 2022).

In the Eastern Alps, a spatial and genetic link of tungsten mineralization with associated metagranitic rocks has now been established for the world-class Felbertal scheelite deposit (Briegleb 1991; Höll and Eichhorn 1998; Kozlik and Raith 2017) located close to the city of Mittersill in Austria (see inset in Fig. 1). However, the majority of subeconomic tungsten occurrences in the Eastern Alps lack such spatial and temporal connection to igneous intrusions. Instead, they form stratabound scheelite mineralization in regional metamorphic metacarbonate or calc-silicate rocks (Wenger 1964; Haditsch and Mostler 1983; Raith 1991). Their stratabound appearance in early Paleozoic volcano-sedimentary sequences led to the postulation of the submarine-exhalative “Sb-W-Hg formation” model, assuming syngenetic/syn-diagenetic mineralization associated with mafic volcanism (Maucher 1965; Höll et al. 1972). Features that did not fit

this model were explained by metamorphic mobilization of tungsten during the Variscan and/or Alpine orogeny (Höll and Eichhorn 1998).

Previous studies have described diverse tungsten mineralization types in the Eastern Alps (Altenberger et al. 2021). Except for the Felbertal scheelite deposit, for which a wealth of radiometric dating is available (for summary see Raith et al. 2018), other tungsten occurrences in the Eastern Alps are not dated. Consequently, their correct genetic contextualization is unknown. Dating of tungsten minerals provides indispensable information for establishing correct genetic models, such as for tungsten deposits in the French Massif Central (Harlaux et al. 2018b; Carr et al. 2021) and the Nanling metallogenic belt, South China (Deng et al. 2019) as well as Au-(Sb)-W deposits in the French Pyrenees (Poitrenaud et al. 2020) and the Stibnite-Yellow Pine district, ID, USA (Wintzer et al. 2022).

This paper focuses on the mineral associations and chemistry of scheelite and ferberite from the Mallnock tungsten deposit in the Eastern Alps. The micro-textures, the trace element compositions, and U–Pb scheelite dates are presented. The more specific objectives of this study are to (i) evaluate the chemistry of scheelite and wolframite of the two ore zones at Mallnock, (ii) use these trace element data to compare element distribution patterns between the two tungstates, (iii) compare these results with those from a global dataset to gain a broader understanding of the chemical signature related to different types of tungsten mineralization, and (iv) constrain the timing of tungsten mineral formation at Mallnock and its inclusion in geodynamic and regional metallogenic contexts along with other ore deposits in the Eastern Alps.

Geology

The tungsten deposit at Mount Mallnock (2,226 m) is located about 11 km SSE of the village of Innerkrems in the Nockberge National Park in the Gurtkal Alps (Fig. 1). It occurs in the uppermost Austroalpine unit of the Drauzug-Gurtkal Nappe System, which is underlain by the Ötztal-Bundschuh Nappe System (Schmid et al. 2004). The complex geological-tectonic configuration is the result of multiple tectonic processes related to the Variscan (Carboniferous; Neubauer et al. 2022) and Eoalpine (Cretaceous; Neubauer et al. 2000) orogenic events.

Several nappes are distinguished in the Mallnock area (Fig. 1). They are part of the Drauzug-Gurtkal Nappe System including, from bottom to top, the Murau, Pfannock, Königstuhl, and Stolzalpe nappes with the latter hosting the Mallnock deposit (Iglseider and Huet 2019; Rantitsch et al. 2020 and references therein). These nappes consist mainly of early Paleozoic low-grade metamorphic

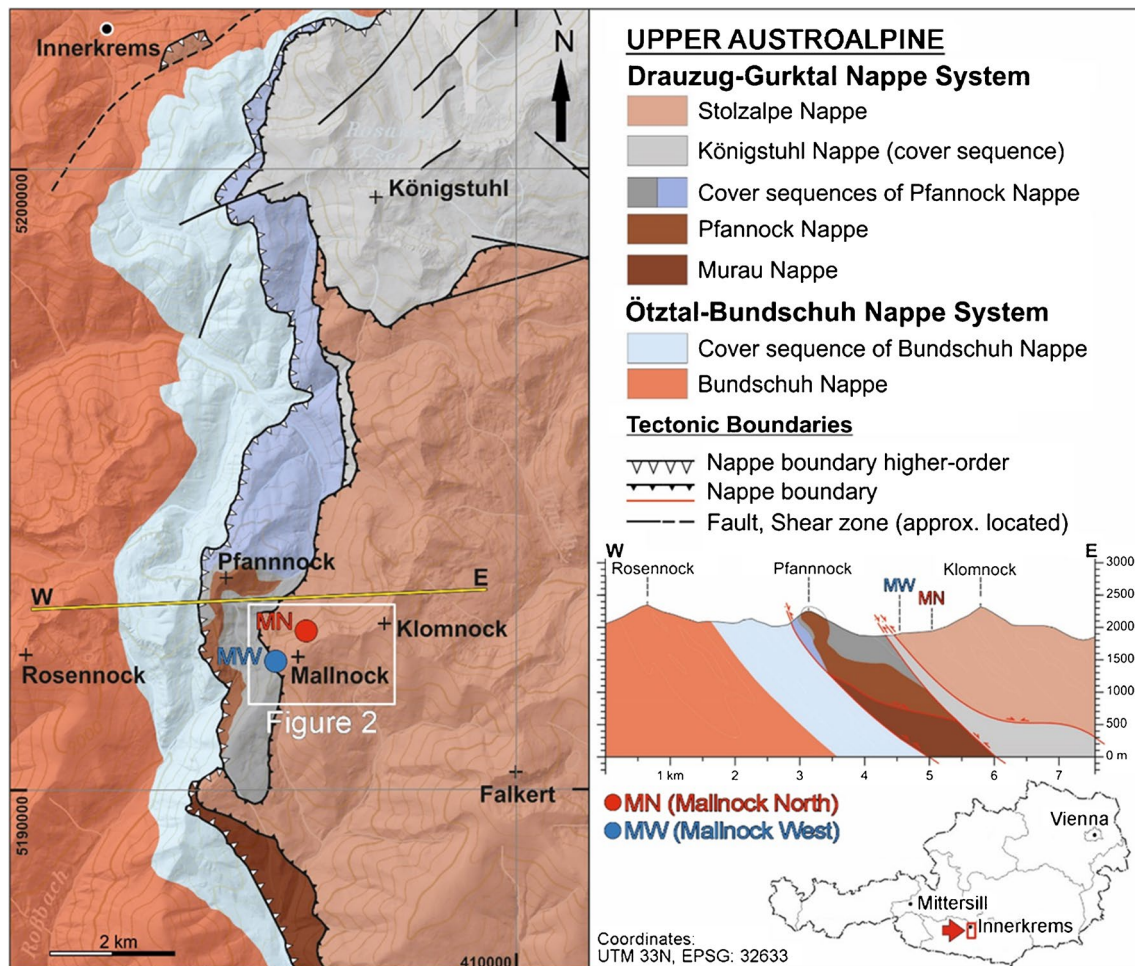


Fig. 1 Tectonic map of the northwestern Gurktal Alps (Iglseider 2019) showing the location of the Mallnock tungsten deposit (MW, Mallnock West; MN, Mallnock North; + symbol, mountain top) and the different tectonic nappes (Paleozoic basement units and Carboniferous to Permo-Mesozoic cover sequences) of the Upper Austroalpine

basement units and Carboniferous to Permo-Mesozoic cover sequences (Fig. 1; Iglseider and Huet 2019; Rantitsch et al. 2020). The basement lithologies comprise meta-volcanic, metasedimentary, and metacarbonate rocks as well as Upper Ordovician metagranitoids (e.g., Pfannock orthogneiss; Iglseider and Huet 2019). The (meta-) sedimentary cover sequences include post-Variscan molasse-type Upper Pennsylvanian siliciclastics and Permian to Upper Triassic carbonate-dominated successions (Fritz and Krainer 2007; Iglseider 2019).

Rocks of the Pfannock and Stolzalpe nappes record Variscan and Eoalpine metamorphism (Neubauer et al. 2019). The volcano-sedimentary sequences in the Stolzalpe Nappe were metamorphosed at temperatures of 300–320 °C (Rantitsch and Rußegger 2000) confirming greenschist facies metamorphic conditions. The Variscan age of low-grade metamorphism is indicated by Lower Pennsylvanian

Drauzug-Gurktal and Ötztal-Bundschuh nappe systems. Background topographic map after BEV (2016). The W-E profile illustrates the placement of the nappes and the tectonic arrangement after Eoalpine nappe stacking (modified after Rantitsch et al. 2020)

$^{40}\text{Ar}/^{39}\text{Ar}$ white mica cooling dates (316 ± 3 Ma; Iglseider et al. 2016).

The (pre-) Variscan structures were overprinted by multi-stage Cretaceous Eoalpine tectonics resulting in regional scale isoclinal folding of the entire nappe pile with coeval top-to-the-W/NW thrusting followed by top-to-the-E/SW normal faulting (see W-E profile in Fig. 1; Iglseider et al. 2016).

At Mallnock, minor metavolcanic (former tuffs and basalts) and metacarbonate rocks are intercalated in the Stolzalpe Nappe (Figs. 2 and 3a; Giese 1988; Iglseider and Huet 2019). At its base, coarse-grained to massive metasandstones with interbedded metasiltstones and (quartz-) phyllites dominate along with thin intercalations of graphitic schists, chlorite-rich phyllites/schists, and greenschists. Higher up in the stratigraphic sequence, ferroan dolomitic rocks (“Eisendolomit”) and banded calcitic marbles become

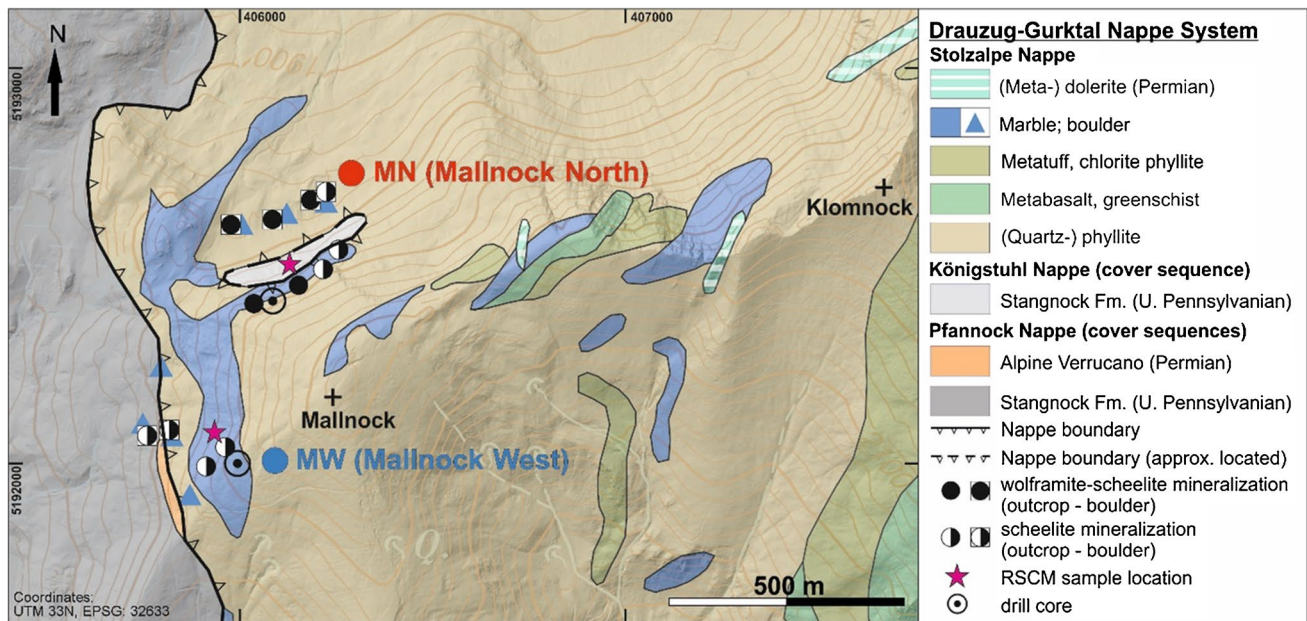


Fig. 2 Geological map of the Mallnock tungsten deposit (modified after Neinavaie et al. 1989; Pistotnik 1996) showing the location of the two main ore zones (Mallnock North, Mallnock West), (meta-) doleritic dikes, and samples collected for Raman spectroscopy of carbonaceous material (RSCM). Background topographic map after BEV (2016)

more prominent. These metacarbonate rocks host the Mallnock deposit. Based on conodont stratigraphy, an Upper Silurian to Lower Devonian stratigraphic age was suggested for the relatively more carbonate-rich sequence (Höll 1970). Porphyritic (meta-) dolerite dikes of Permian age that have been dated in this study (see results below) are exposed NE of Mallnock striking SW-NE to W-E (Fig. 2; Giese 1988; Pistotnik 1996; Iglseider et al. 2019).

Tungsten mineralization at Mallnock

In 1981, alluvial prospecting for tungsten minerals in combination with systematic geochemical analysis of stream sediments indicated an anomaly in the Nockberge area with W contents > 130 µg/g (Thalman et al. 1987). Subsequent exploration including night prospecting with ultraviolet (UV) lamps led to the discovery of scheelite-ferberite mineralization at Mallnock (Neinavaie 1984). Tungsten-mineralized rocks are restricted to tectonically disrupted layers of Fe-bearing magnesite-dolomite rocks within phyllites of the Stolzalpe Nappe (Neinavaie et al. 1989). The carbonate-rich ore horizon is exposed at an elevation of ca. 2060 and 2100 m on the western and northern slopes of Mallnock, respectively, and separated by talus deposits and boulders, dividing the deposit into two ore zones: Mallnock West and Mallnock North (Figs. 1, 2, 3b). Exploration between 1981 and 1987, including trenching and drilling, revealed that the moderately ESE-dipping ore horizon can be traced

over a distance of about 700 m along strike and consists of several 0.5 to 3.5 m thick, tungsten-bearing carbonate layers. Average tungsten contents were estimated at 0.8 mass% WO₃ (Mallnock North, 0.9 mass% WO₃; Mallnock West, 0.5 mass% WO₃), representing a total resource of about 2800 t WO₃ (Thalman and Ronge 1987).

The host rocks comprise mainly Fe-magnesite and dolomitic marble. The Fe-magnesite occurs as coarse-grained to sparry, light yellowish-brown rock with a massive to slightly schistose texture and contains a younger generation of minor white, coarse-grained dolomite (Fig. 3d, f). A distinct zoning of Fe-magnesite crystals has been determined by electron probe microanalysis (EPMA) with about 10.4 mass% FeO in the core and an increase towards the rims of up to 15.5 mass% (Neinavaie et al. 1989). Typical metasomatic replacement features are apparent at the magnesite-dolomite contacts. The fine-grained dolomitic marble has a notably uniform chemical composition with relatively low FeO contents between 0.7 and 2.9 mass% (Neinavaie et al. 1989). Commonly, sedimentary bedding and thin layers of graphitic schist are visible.

At Mallnock West, scheelite occurs in irregularly oriented millimeter-thin veinlets that merge into a delicate stockwork mineralization and as centimeter-large scheelite aggregates. Scheelite is hosted primarily in dolomitic marble containing minor Fe-rich magnesite crystals (Fig. 3c, e). In contrast, mineralization at Mallnock North is characterized by the association of scheelite with ferberite in Fe-magnesite. Both tungsten minerals are present as fissure fillings and clusters

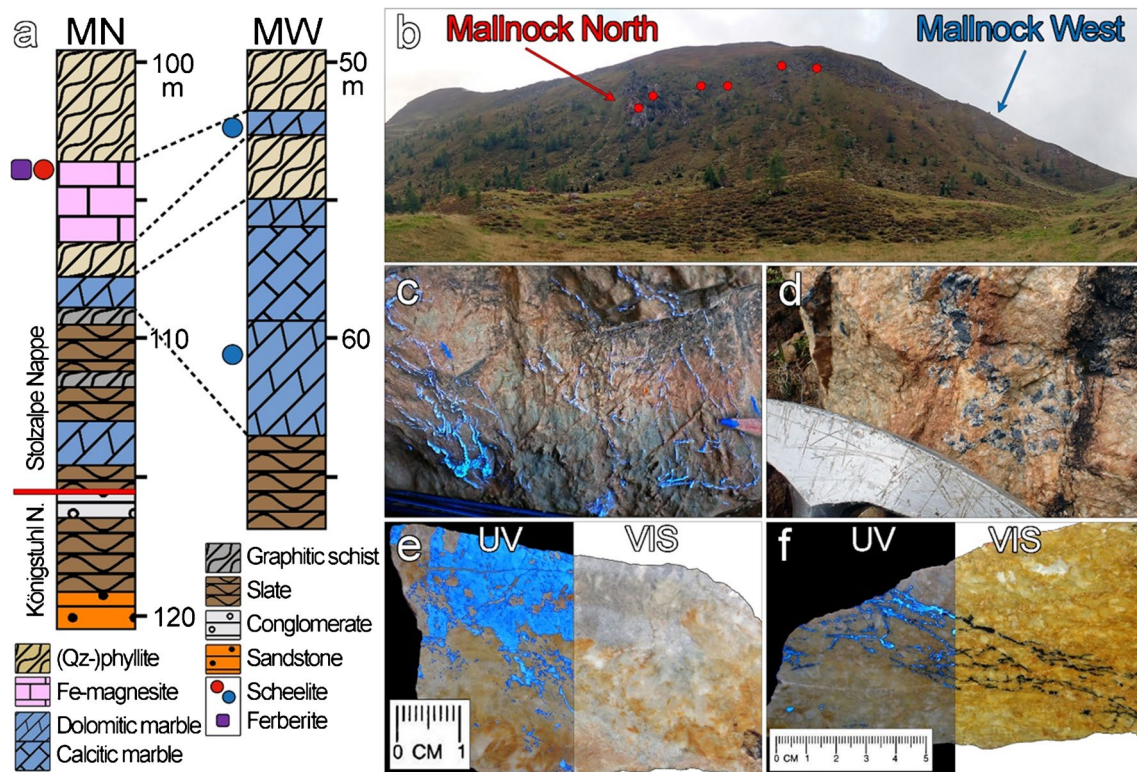


Fig. 3 Local geology and mineralization style at Mallnock. **a** Schematic redrawing of two drill cores from Mallnock (MN, Mallnock North; MW, Mallnock West) showing the simplified stratigraphy of the mineralized rock series; modified from Neinavaie et al. (1989). **b** Scenic view of the Mallnock area and indicated outcrops (red circles) of the scheelite-ferberite mineralization at Mallnock North. Mallnock West is at the backside of the hill. **c** Stockwork-like scheelite veinlets

(pale blue fluorescence color) in ferroan dolomite, Mallnock West. Photo taken with combined daylight (VIS) and short-wave ultraviolet (UV) light. **d** Cluster of ferberite (black) in sparry Fe-magnesite. Ferberite is marginally surrounded by white scheelite, Mallnock North. **e–f** Hand specimens under UV and VIS with **e** showing massive scheelite in ferroan dolomite from Mallnock West and **e** veinlets of scheelite-ferberite in Fe-magnesite from Mallnock North

up to a few millimeters in size. In irregular veinlets and fissure fillings, ferberite is surrounded by thin scheelite fringes (Fig. 3d, f). Millimeter-sized subhedral to euhedral scheelite crystals mostly contain anhedral ferberite in the core zones (Fig. 4b, d–e). Thin quartz veinlets with minor scheelite intersect the ferberite-scheelite stockwork and were interpreted as a subsequent stage of minor tungsten precipitation (Neinavaie et al. 1989). Scheelite at Mallnock exhibits blue fluorescence throughout in short-wave UV light, indicating a paucity of Mo (Fig. 3c, e–f).

Sampling and analytical methods

For this study, we used specimens collected during recent field campaigns as well as archived samples stored in the collections of GeoSphere Austria and Montanuniversität Leoben. A total of six polished blocks and six polished thin sections containing scheelite (Mallnock West) and scheelite-ferberite (Mallnock North), respectively, were prepared and used for analytical studies. In the following,

an overview of the applied methods and instrument settings is given. A list of the samples and additional details about the analytical procedure and data processing are enclosed in the electronic supplementary material 1 (ESM 1).

Mineral liberation analysis (MLA) was conducted at the Helmholtz Institute Freiberg for Resource Technology (Germany) using a ThermoFisher Quanta 650F MLA system equipped with two Bruker Quantax X-Flash 5030 energy-dispersive X-ray (EDX) detectors. False color images were created by combining backscattered electron (BSE) images and EDX analyses using FEI's MLA suite, version 3.1.4. Further information regarding the measurement procedure can be found in Bachmann et al. (2017). The complete set of MLA images is included in ESM 2a.

Major and minor element contents in scheelite and ferberite were determined by EPMA using a JEOL JXA 8200 superprobe at the Chair of Resource Mineralogy at Montanuniversität Leoben (Austria) and a JEOL JXA 8530F Hyperprobe at the Helmholtz Institute Freiberg for Resource Technology. Conditions for analyses were 20 kV

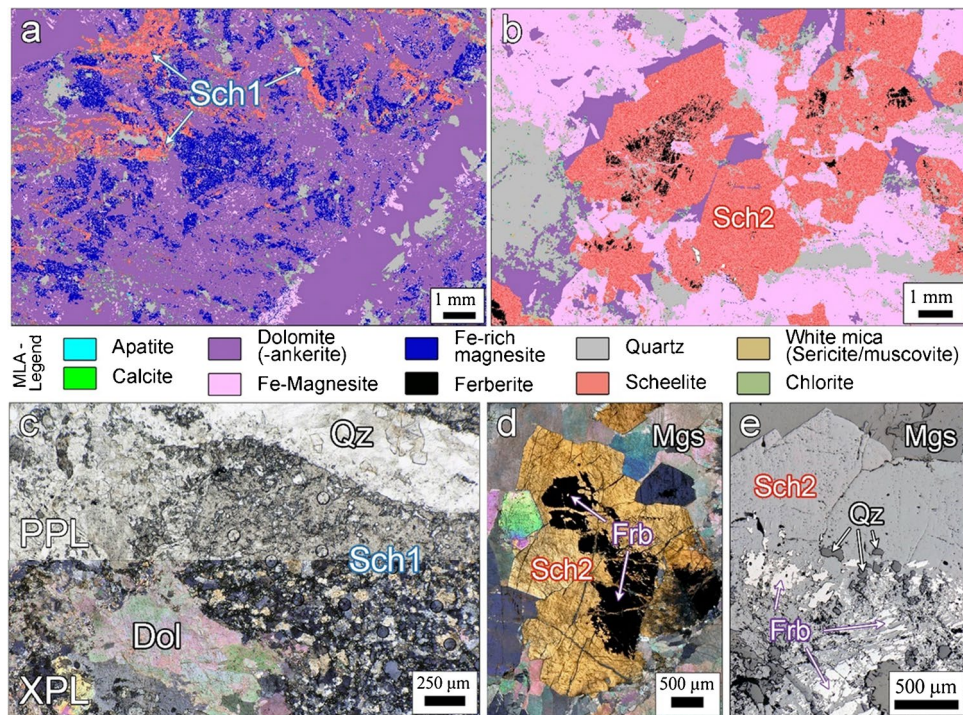


Fig. 4 Mineral distribution maps and photomicrographs of Mallnock West (**a**, **c**) and Mallnock North (**b**, **d–e**). **a** MLA map of sample MA-W-1 from Mallnock West showing schlieren-like scheelite (Sch1) in dolomite(-ankerite) and Fe-rich magnesite (see MLA legend for color code). **b** MLA map of sample MA-N-1 from Mallnock North with scheelite crystals (Sch2) containing relict ferberite in the center parts. The tungsten minerals are embedded in Fe-magnesite, dolomite(-ankerite), and quartz. **c** Photomicrograph of a frayed end of a lenticular Sch1 aggregate under transmitted light (TL); upper

half with plane-polarized light (PPL), lower half with cross-polarized light (XPL). The XPL section highlights the mosaic fabric of fine-crystalline Sch1 subgrains, sample MA-W-1A. **d** Subhedral Sch2 (yellow interference color) with opaque ferberite in the center surrounded by Fe-magnesite, sample MA-N-2, TL (XPL). **e** Reflected light (PPL) photomicrograph of a euhedral Sch2 (light gray) with corroded ferberite (white) in the central part surrounded by Fe-magnesite (dark gray); sample MA-N-1. Mineral abbreviations: Dol = dolomite, Frb = ferberite, Mgs = Fe-magnesite, Sch = scheelite, Qz = quartz

acceleration voltage, 10–100 nA probe current, and a beam diameter of 1–2 μm .

Trace element analysis of scheelite and ferberite was conducted on a Thermo Fisher Element XR sector field ICP-MS coupled to a Teledyne Photon Machines Analyte G2 193-nm ArF excimer laser ablation system at the Institute for Mineralogy at Westfälische Wilhelms-Universität Münster (Germany). All analyses were performed using a uniform spot size of 40 μm at 10 Hz with energy of ca. 4 J/cm². The reference materials include the glass standards NIST612 (used as external reference material; Jochum et al. 2011), GSD-1G, GSE-1E (Guillong et al. 2005; Jochum et al. 2005), and three matrix-matched in-house reference materials collected from the Felbertal scheelite deposit (Scheelite-A, Scheelite-B, and Scheelite-S). Trace element data processing and evaluation were performed using the software G.O.Joe (<https://gojoe.software>) in order to correct the abundance sensitivity of W on Ta and Re.

Two samples (MA-N-1A from Mallnock North and MA-W-1A from Mallnock West) were selected for U–Pb radiometric dating. Scheelite LA-ICP-MS in situ U–Pb analyses

were performed with a Teledyne Photon Machines Analyte 193-nm ArF excimer laser ablation system coupled to a Thermo Fisher Element 2 high-resolution ICP-MS at the Radiogenic Isotope and Geochronology Laboratory at the School of the Environment, Washington State University (USA). Isotopic ratios of U, Th, and Pb in scheelite were acquired using an 80 μm beam diameter firing at 10 Hz and a fluence of about 4 J/cm². The matrix-matched natural scheelite reference material NMNH-107667 (ID-TIMS reference age, 57.52 \pm 0.22 Ma; Wintzer 2019; Wintzer et al. 2022) was used as primary external reference material together with the wolframite reference material YGX-2107 (ID-TIMS reference age, 161.3 \pm 0.8 Ma; Yang et al. 2020) as monitor and for ²⁰⁷Pb/²⁰⁶Pb ratio calibration. Data reduction included standard background subtraction and fractionation correction (Horstwood et al. 2016; Wintzer et al. 2020) using Iolite 4 (<https://iolite-software.com>; Paton et al. 2011). In Iolite, the UcomPbine V3 DRS (data reduction scheme) was used followed by the 207-correction from Chew et al. (2014). Tera-Wasserburg concordia plots were generated with IsoplotR (v5.5; Vermeesch 2018) that

calculates reliable ages using model 2 meaning total least squares with no MSWD reported.

Whole-rock chemistry of five samples of (meta-) dolerite dikes was conducted by Activation Laboratories Ltd. (Ancaster, Ontario, Canada). Apatite of one dike sample (Rinsennock, about 6 km NE of Mallnock) was separated for U–Pb radiometric dating. The ratios of $^{206}\text{Pb}/^{238}\text{U}$, $^{207}\text{Pb}/^{235}\text{U}$, and $^{207}\text{Pb}/^{206}\text{Pb}$ were determined by LA-MC-ICP-MS techniques with a NewWave 193-nm ArF excimer laser coupled to a Nu Plasma II mass spectrometer at the NAWI Graz Geocenter (Austria). Limiting error corrections were accepted using zircon standards GJ1 as primary external reference material (Jackson et al. 2004); 91500, Plešovice, and NIST612 were used as secondary reference materials (Wiedenbeck et al. 1995; Jackson et al. 2004; Sláma et al. 2008). Tera-Wasserburg concordia plots were generated with IsoplotR (v5.5; Vermeesch 2018) using the maximum likelihood formulation of Ludwig (1998).

Raman spectroscopy of carbonaceous material (RSCM) was performed at Montanuniversität Leoben using a Horiba LabRam HR Evolution 800 instrument equipped with a $\times 100$ distance objective lens. Ordering of carbon in the sheet structure of carbonaceous matter (semigraphite, graphite) is temperature sensitive and the numerical analysis of its Raman spectra is used for temperature estimations (Beyssac et al. 2002). The carbonaceous matter was isolated from the organic-rich metasedimentary rocks by acid treatment. For each sample, about 20 spectra were recorded by two scans with an acquisition time of 20 s in the 700–2,000 cm^{-1} region. Further details on the analytical techniques and calibration for RSCM are described in Rantitsch et al. (2020). RSCM data were calculated according to Lünsdorf et al. (2017).

Results

Mineralogy and micro-textures

The samples from Mallnock West are composed of Fe-free to ferroan dolomite ($X_{\text{Fe}} = 0$ to 0.25) and Fe-rich magnesite ($X_{\text{Fe}} = 0.3$ to 0.5) with minor scheelite and quartz. Accessory minerals include apatite, calcite, sericite, chlorite, and pyrite. Fe-rich magnesite, scheelite, and quartz form irregular patches to stringer-like accumulations in fine-grained (0.1 to 2 mm) dolomite, which are crosscut by younger carbonate-quartz veinlets (Fig. 4a). The carbonate mineralogy is complex. Magnesite crystals intergrown with dolomite are anhedral and Fe-rich ($X_{\text{Fe}} \approx 0.3$ to 0.5), whereas those in the dolomite-quartz veinlets tend to be of rhombohedral shape with lower Fe contents ($X_{\text{Fe}} \approx 0.25$; Fig. 4a).

Scheelite 1 (Sch1) at Mallnock West forms an irregular network of 0.05 to 1 mm thick fissures and centimeter-sized

elongated scheelite aggregates (Fig. 4a), which display brittle/ductile deformation indicators, such as undulose extinction and micro-fractures. Veinlets and aggregates consist of fine-crystalline (5–50 μm) scheelite subgrains developing a mosaic-like recrystallization fabric (Figs. 4c and 5a–b). In places, larger scheelite crystals preserve primary growth zoning and show transitions into CL brighter and more homogeneously textured fine-grained scheelite towards the margins (Fig. 5a). Some of the subgrains in thin veinlets consist of darker luminescent cores, which become brighter towards the edges (Fig. 5b). The micro-textural features of relict growth zoning and dark CL cores in Scheelite 1 suggest that an early subtype Scheelite 1a (Sch1a) was overprinted by a later subtype Scheelite 1b (Sch1b) at a subsequent stage of mineralization.

Samples from Mallnock North contain 60–80 vol% Fe-magnesite (i.e., breunnerite; $X_{\text{Fe}} = 0.1$ to 0.3) with variable amounts of ferroan dolomite, quartz, scheelite, and ferberite (Fig. 4b). Minor and accessory phases comprise sericite, apatite, calcite, chlorite, titanite, rutile, and pyrite. Fe-magnesite occurs as very fine-grained masses, with crystals less than 1 mm, and as coarse crystals up to 1 cm in size. Fine-grained Fe-magnesite is predominantly anhedral to subhedral developing mosaic-like fabrics (Fig. 4d). In contrast, larger Fe-magnesite crystals develop well-defined rhombohedra showing undulose extinction. Dolomite occurs subordinately in the recrystallized matrix and forms euhedral crystals up to several cm in size associated with Fe-magnesite and scheelite (Fig. 4b). Locally, it is in direct contact with scheelite and forms thin veinlets in cataclastic ferberite and scheelite (Fig. 4d).

Ferberite is only present at Mallnock North and occurs within Fe-magnesite (Fig. 3d, f). It forms anhedral crystals in the cores of clusters and in stockwork-like veinlets and is commonly replaced by Scheelite 2 (Sch2) from Mallnock North. Scheelite 2 displays larger (3–5 mm) crystals and appears free of ferberite at the outer grain area (Fig. 4d–e). The scheelite micro-texture is homogeneous in CL and, along with ferberite, documents minor cataclastic deformation represented by dolomite-healed microcracks in both minerals (Figs. 4d, 5c). Textural features indicate that only one type of ferberite is present, which is overgrown and replaced by one type of Scheelite 2.

Major and minor element compositions of scheelite and ferberite

Mineral chemical data are listed in ESM 3a. Scheelite contains almost stoichiometric CaO (mean $\text{CaO} = 19.4 \pm 0.2$ mass%) and WO_3 (mean $\text{WO}_3 = 81.2 \pm 0.8$ mass%). Ferberite also has stoichiometric values of WO_3 (mean $\text{WO}_3 = 77.2 \pm 0.4$ mass%) and much higher contents of

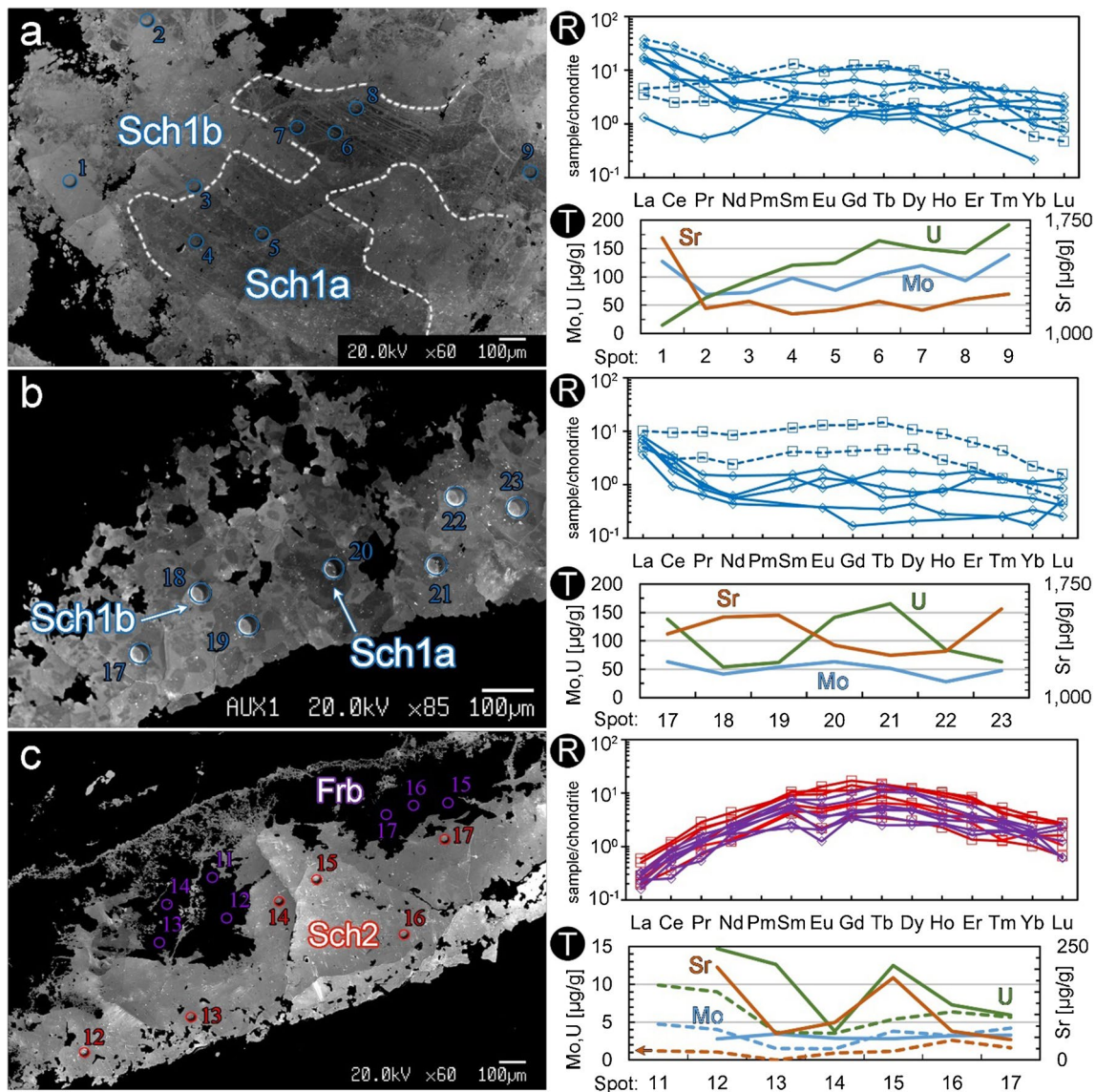


Fig. 5 Cathodoluminescence (CL) images of scheelite from Mallnock West (Sch1, **a–b**) and Mallnock North (Sch2, **c**) with corresponding REE_{CN} plots (R) and trace element contents (T) to the right. **a** Sch1 from Mallnock West showing its micro-textural subtype Sch1a with primary zoning (stripe pattern of dark luminescence) and a transition into homogeneous CL brighter and fine-crystalline subtype Sch1b at the margin (blue circles indicate laser ablation spots), sample MA-W-1. R-REE_{CN} plots of the corresponding analysis spots (solid lines, Sch1a; dashed lines, Sch1b). T-Trace element contents correspond to the laser ablation spots numbered in **a**. **b** Veinlet with Sch1 aggregate

showing dark (Sch1a) and bright (Sch1b) luminescence. R-REE_{CN} plots of the corresponding analysis spots (solid lines, Sch1a; dashed lines, Sch1b). T-Trace element contents correspond to the laser ablation spots numbered in **b**. **c** Section of a scheelite-ferberite veinlet consisting of ferberite in the center that is replaced by Sch2 exhibiting a homogeneous CL-texture, sample MA-N-1. R-REE_{CN} plots of the corresponding analysis spots (red, Sch2; purple, ferberite). T-Trace element contents correspond to laser ablation spots numbered in **c** (solid lines, Sch2; dashed lines, ferberite, note that Sr for ferberite is shown on the left y-axis)

FeO (mean FeO = 21.4 ± 0.8 mass%) than MnO (mean MnO = 0.9 ± 0.2 mass%), corresponding to a mean composition of 96.0 ± 0.8 mol% ferberite (FeWO_4) in the solid solution series with hübnerite (MnWO_4). Other minor elements detectable by EPMA in ferberite are Mg and Mn with mean contents of 4120 and 6560 $\mu\text{g/g}$, respectively (Table 1).

Trace element compositions of scheelite

Scheelite from Mallnock incorporates quantifiable (by LA-ICP-MS) amounts of Na, Mg, Mn, As, Sr, Y, Nb, Mo, Ba, rare earth elements (REE), Hf, Pb, Th, and U. The trace element distribution and REE patterns of scheelite and ferberite are illustrated in Figs. 6 and 7. A summary of selected trace

Table 1 Summary statistics of selected trace elements in scheelite and ferberite from Mallnock determined by LA-ICP-MS

Ore zone	Mallnock West						Mallnock North											
	Scheelite 1						Scheelite 2						Ferberite					
	Element (µg/g)	Mean	n%	C.I. Min	C.I. Max		Mean	n%	C.I. Min	C.I. Max		Mean	n%	C.I. Min	C.I. Max			
Na	91.8	100	75.3	112	30.6	80	16.6	56.4	30.0	78	19.1	47.3						
Mg	20.9	100	15.9	27.5	14.5	92	7.55	27.8	4,120	100	3730	4540						
Mn	0.865	95	0.467	1.60	1.15	74	0.450	2.95	6,560	100	5950	7230						
Sr	1270	100	1250	1280	119	100	58.8	241	1.08	96	0.862	1.35						
Y	13.0	100	8.78	19.4	5.03	100	2.60	9.75	0.602	98	0.321	1.13						
Nb	0.486	100	0.470	0.502	0.484	100	0.450	0.521	0.789	100	0.741	0.841						
Mo	52.6	100	48.7	56.9	0.894	96	0.532	1.50	1.04	97	0.571	1.88						
Ba	7.60	100	4.14	14.0	3.41	92	1.19	9.80	3.31	98	2.26	4.86						
La	2.51	100	1.71	3.68	0.0790	98	0.0376	0.166	0.0117	71	0.0045	0.0307						
Ce	5.09	100	3.22	8.06	0.446	98	0.215	0.925	0.0540	83	0.0171	0.170						
Pr	0.675	100	0.404	1.13	0.0853	89	0.0359	0.203	0.0131	50	<0.011	0.0340						
Nd	2.85	100	1.87	4.33	0.575	88	0.241	1.37	0.0932	53	<0.063	0.284						
Sm	0.862	91	0.794	0.936	0.339	70	0.136	0.846	0.0848	46	<0.074	0.215						
Eu	0.338	93	0.285	0.402	0.229	80	0.0862	0.610	0.0230	54	<0.015	0.0582						
Gd	1.34	95	0.873	2.05	0.864	93	0.379	1.97	0.119	67	<0.053	0.324						
Tb	0.230	95	0.143	0.371	0.171	96	0.0819	0.356	0.0250	75	0.0097	0.0637						
Dy	1.61	100	1.05	2.47	1.06	97	0.517	2.16	0.205	90	0.0791	0.529						
Ho	0.273	98	0.163	0.458	0.171	95	0.0810	0.360	0.0324	82	0.0128	0.0815						
Er	0.589	93	0.271	1.28	0.398	91	0.188	0.845	0.0903	79	0.0397	0.205						
Tm	0.0597	91	0.0489	0.0730	0.0392	81	0.0201	0.0765	0.0118	58	<0.007	0.0221						
Yb	0.215	91	0.0985	0.469	0.207	82	0.0934	0.461	0.0780	70	0.04884	0.124						
Lu	0.0292	98	0.0262	0.0325	0.0296	76	0.0153	0.0572	0.00972	50	<0.008	0.0116						
Hf	0.407	100	0.370	0.449	0.145	79	0.0530	0.399	0.0598	67	0.0513	0.0698						
Ta	<0.008	35	n.d	n.d	<0.008	11	n.d	n.d	<0.011	7	n.d	n.d						
Pb	5.66	100	4.65	6.89	1.91	100	0.758	4.80	1.40	99	0.784	2.48						
Th	0.255	95	0.186	0.348	0.491	99	0.354	0.682	0.449	97	0.252	0.801						
U	78.67	100	66.2	93.4	31.8	100	23.0	43.9	11.1	100	8.41	14.6						
REE+Y	33.0		23.1	47.2	10.5		5.13	21.4	1.75		0.840	3.64						

Mean, geometric mean; n%, percentage of measurements above LOD; C.I. Min, lower bound of the 95% confidence interval of the mean; C.I. Max, upper bound of the 95% confidence interval of the mean; n.d., not determined

Fig. 6 Spider diagrams showing trace element distribution of scheelite and ferberite. **a** Trace element content of scheelite from Mallnock West (Sch1) and Mallnock North (Sch2) normalized to the mean of all scheelite analyses from Mallnock. **b** Trace element composition of ferberite normalized to the mean composition of Sch2. **c** Comparison of ferberite from Mallnock North to the mean composition of global wolframite group data by Goldmann (2016)

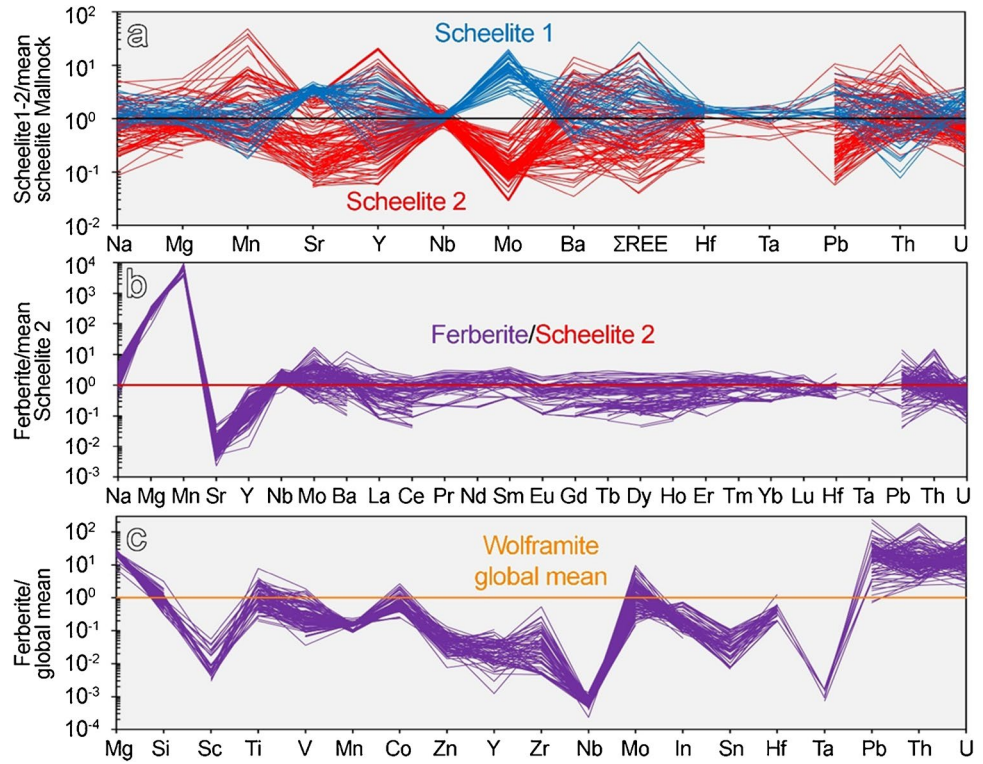
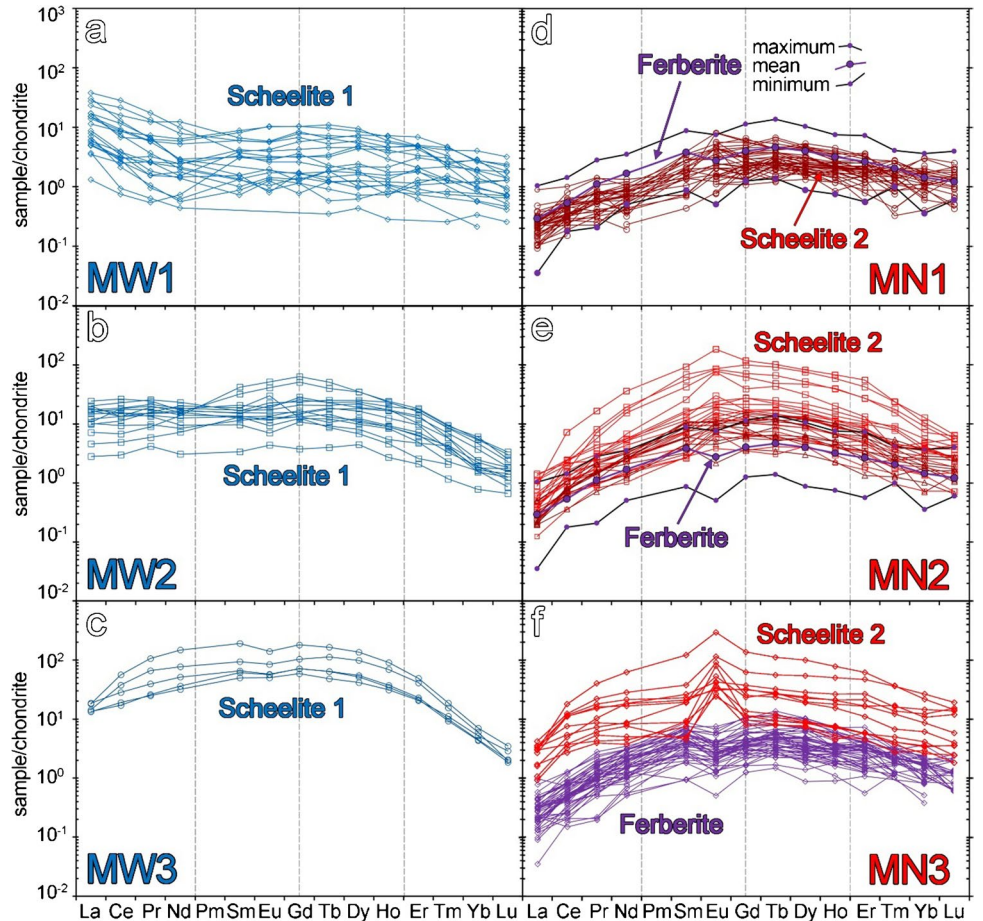


Fig. 7 Scheelite and ferberite REE contents normalized to chondrite values (McDonough and Sun 1995). Different subtypes of REE patterns of scheelite for Mallnock West (Sch1, blue, **a–c**) and Mallnock North (Sch2, red, **d–f**); see text for details. Ferberite data (mean with minimum and maximum) from Mallnock North are included in **d–f**



elements is given in Table 1 and the entire dataset, including Pearson correlation coefficients, is provided in ESM 3b-c.

Differences in the distribution of Na, Sr, and particularly Mo for Scheelite 1 from Mallnock West and Scheelite 2 from Mallnock North are noted (Table 1). Although the Mo contents in scheelite from Mallnock are generally very low (range 0.2–138 µg/g), they are higher in Scheelite 1 (Fig. 6a). Strontium also shows higher contents and lesser variability in Scheelite 1 than in Scheelite 2 (Fig. 6a). The values of Na are variable showing a considerable overlap.

High U contents are characteristic for scheelite from Mallnock (Table 1, Fig. 6a). In Scheelite 1, the mean U content is 79 µg/g, in Scheelite 2, it is 32 µg/g. The contents of Th (<0.68 µg/g) are much lower and similar in scheelite from the two ore zones. The contents of Pb, Mg, Mn, Nb, Ta, Ba, and Hf are also similar (Table 1, Fig. 6a). Niobium is generally only present in small quantities in Scheelite 1 and Scheelite 2 (ca. 0.5 µg/g) but was above the lower limit of detection (LOD) in all analyses. In contrast, Ta is below the LOD (ca. 1×10^{-2} µg/g) in about 50% of the analyses. The remaining analyses yielded Ta contents up to 0.2 µg/g Ta in Scheelite 1.

There is a considerable variation of the Σ REE and Y contents (Table 1, Fig. 6a). The distribution of REE in scheelite from Mallnock is illustrated in chondrite-normalized (REE_{CN}) diagrams (Fig. 7a–f). The REE patterns of Scheelite 1 and 2 are different. They can be distinguished in respect of their ΣREE_{CN} , REE_{CN} ratios (i.e., $[La/Nd]_{CN}$, $[Gd/Lu]_{CN}$) and europium (Eu) anomaly (i.e., $Eu_A = Eu_{CN}/Eu^*_{CN}$, where $Eu^*_{CN} = [Sm_{CN} \times Gd_{CN}]^{0.5}$).

Particularly, Scheelite 1 from Mallnock West shows differences in its REE distribution allowing the distinction of three subtype patterns (Fig. 7a–c). The MW1 patterns are more abundant in Scheelite 1a and characterized by the domination of light REE (LREE; $[La/Nd]_{CN} = 5.1 \pm 3.4$) and the lowest total REE contents (ΣREE_{CN} 8 to 130, Fig. 7a). The Eu anomaly shows small negative as well as positive Eu_A values ($Eu_A = 0.49$ to 1.68). The MW2 patterns have a more even distribution of LREE and intermediate REE (MREE) and present low heavy REE (HREE) values with flat to slightly convex LREE-MREE ($[La/Nd]_{CN} = 1.0 \pm 0.4$, $[Gd/Lu]_{CN} = 13 \pm 6.3$; Fig. 7b). The Eu anomaly is also not very pronounced ($Eu_A = 0.69$ to 1.96). Scheelite patterns MW3 have the highest ΣREE_{CN} values ranging from 408 to 1307 (Fig. 7c). This rare subtype exhibits distinct convex REE patterns with the highest MREE contents ($[La/Nd]_{CN} = 0.3 \pm 0.1$, $[Gd/Lu]_{CN} = 39 \pm 13$) and slightly negative Eu anomalies ($Eu_A = 0.85 \pm 0.06$). The MW2 and MW3 patterns are more common in Scheelite 1b. One common feature of REE patterns MW1–MW3 is the predominance of the LREE over the HREE ($[La/Lu]_{CN} = 3$ to 23).

The REE patterns of Scheelite 2 from Mallnock North are similar but show lower LREE contents than at Mallnock

West. The patterns are also classified into three different subtypes for descriptive purposes (Fig. 7d–f). Subtype MN1 has the lowest ΣREE_{CN} values (3.9 to 43) and forms slightly bell-shaped to sinistral inclined patterns ($[La/Nd]_{CN} = 0.43 \pm 0.3$, $[Gd/Lu]_{CN} = 2.4 \pm 2.2$; Fig. 7d). The mean Eu_A of 1.3 ± 0.5 is positive with only a few negative values (0.74 to 0.86). Subtype MN2 has higher ΣREE_{CN} values (26 to 858) and exhibits distinctive bell-shaped patterns characterized by low LREE contents ($[La/Nd]_{CN} = 0.15 \pm 0.1$) and stronger MREE fractionation ($[Gd/Lu]_{CN} = 6.9 \pm 4.1$) compared to subtype MN1 (Fig. 7d–e). This subtype shows positive as well as negative Eu anomalies. The patterns with negative Eu_A values commonly have lower ΣREE_{CN} and overlap with the REE patterns of ferberite (Fig. 7e). The MN3 patterns include the highest total REE contents ($\Sigma REE_{CN} = 95$ to 1095). They exhibit slightly to distinctive bell-shaped patterns with low LREE contents ($[La/Nd]_{CN} = 0.05$ to 0.67, mean 0.25; $[Gd/Lu]_{CN} = 2.1$ to 9.4, mean 4.2) and distinct positive Eu anomalies ($Eu_A = 1.1$ to 8.0; Fig. 7f).

Trace element composition of ferberite

Trace element contents of ferberite are presented and compared to those of Scheelite 2 from Mallnock North where the two minerals are intimately intergrown (Table 1, Fig. 6b). Similar to scheelite, ferberite from Mallnock incorporates quantifiable amounts of Ti, V, Co, Zn, Zr, and In (Fig. 6c). A remarkable feature is the very low Sr content in ferberite (mean 1.1 µg/g). The mean contents of Mo (1.0 µg/g) and Nb (0.8 µg/g) are low but similar to Scheelite 2 (Table 1, Fig. 6b). Tantalum is only detectable in 7% of the ferberite measurements; the few values above the LOD are comparable to those of Scheelite 2.

The mean content of U is 11 µg/g, which is significantly lower than in Scheelite 2 (Table 1, Fig. 6b). The contents of Pb and Th are very similar with about 1.4 µg/g and 0.5 µg/g, respectively. The mean values for Na and Ba are 30 µg/g and 3.3 µg/g, respectively, and close to that of Scheelite 2. In comparison to the mean composition of wolframite from a global dataset of primarily granitic magmatic-hydrothermal and pegmatitic tungsten deposits (Goldmann 2016), most of the trace elements, especially Nb and Ta, of the Mallnock ferberite are strongly depleted, whereas U, Th, Pb, Mg, and to some extent Mo are enriched (Fig. 6c).

The Σ REE in ferberite range from 0.04 to 11.2 µg/g (mean 1.8 µg/g) but some REE are only above the LOD in 45–50% of the measurements (Table 1). For the individual REE, mean contents between 0.01 and 0.2 µg/g were obtained. Compared to Scheelite 2, REE contents are generally slightly lower in ferberite and Eu shows a distinct negative anomaly (Table 1, Fig. 6b). Ferberite generally shows uniform patterns (Fig. 7d–f). However, about 50% of the analyses had to be discarded because of too low contents of

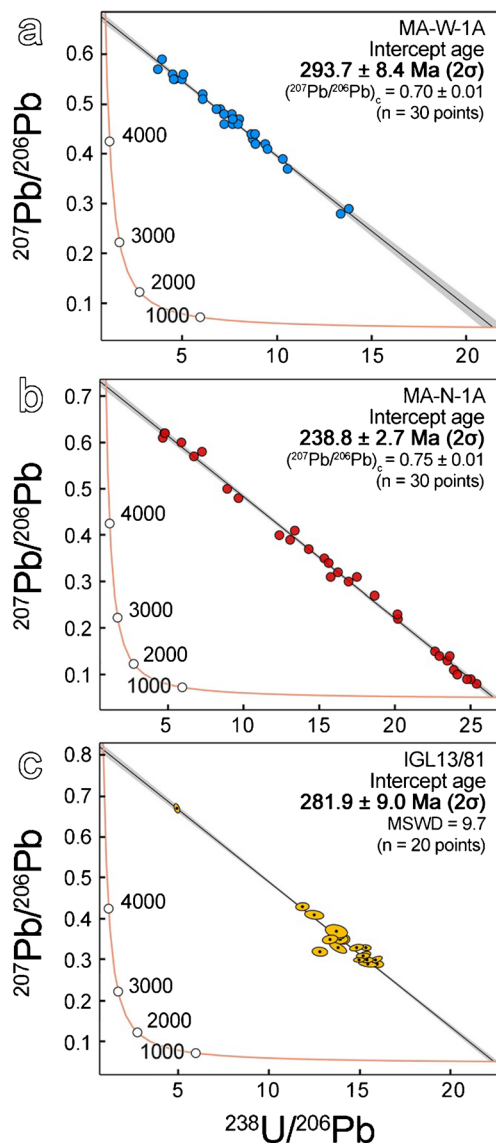


Fig. 8 Tera-Wasserburg diagrams illustrating U–Pb data of (a) Scheelite 1-Mallnock West and (b) Scheelite 2-Mallnock North. c Apatite U–Pb data from a monzodiorite dike at Mount Rinsennock. Calculations were made with IsoplotR (v5.5; Vermeesch 2018)

several REE (particularly Pr, Nd, Sm, Eu, and Lu). Those patterns that were not excluded are bell-shaped and sinistral inclined ($[La/Nd]_{CN} = 0.2 \pm 0.1$, $[Gd/Lu]_{CN} = 2.9 \pm 2.5$, $[La/Lu]_{CN} = 0.02$ to 0.5), mostly with negative Eu_A values (mean 0.7 , 0.4 – 1.2). Ferberite patterns resemble MN1 and MN2 patterns of Scheelite 2 showing negative Eu_A values (Fig. 7d–e) and clearly differ from Scheelite 1 (Fig. 7a–c).

In situ U–Pb scheelite dating

The U–Pb isotopic data for the samples and reference materials used for this study are included in ESM 4a. The dataset for Scheelite 1 (sample MA-W-1A) plotted on a

Tera-Wasserburg diagram defines a regression line that yields a lower-intercept date of 293.7 ± 8.4 Ma (2σ , $n = 30$; Fig. 8a). The U–Pb date for Scheelite 2 (sample MA-N-1A) was determined by a well-defined lower-intercept of 238.8 ± 2.7 Ma (2σ , $n = 30$; Fig. 8b). U–Pb scheelite data points plot tightly as mixing array with the regression nested within the points. Both dates are based on a robust dataset of 30 points and the uncertainty ranges are less than 3%.

Whole-rock chemistry and dating of dikes

A detailed petrographic and chemical characterization of the studied dike rocks is provided in ESM 2c and ESM 3d. The five samples have intermediate SiO_2 contents and are classified as monzodiorite and gabbro diorite showing calc-alkaline signatures. The samples are strongly enriched in LREE and depleted in HREE showing dextral inclined REE patterns with weakly negative Eu anomalies.

To determine an event-based age of the dikes, a suitable apatite crystal was selected after no dateable-sized zircons could be found. The results of U–Pb radiometric dating of apatite define a regression line on a Tera-Wasserburg diagram that yields a lower-intercept date of 281.9 ± 9.0 Ma (2σ , $n = 20$, MSWD = 9.7), indicating an early Permian (Cisuralian) intrusion of this monzodioritic dike from Rinsennock. The complete dataset is provided in ESM 4b.

Raman spectroscopy of carbonaceous material

Two samples containing carbonaceous material were analyzed (Fig. 2). A metasandstone of the lowermost Königstuhl Nappe about 500 m away from Mallnock yielded a median maximum temperature of 258 ± 27 °C ($n = 20$). A dolomitic marble of the overlying Stolzalpe Nappe yielded 296 ± 27 °C ($n = 19$). This dolomitic marble horizon hosts the scheelite at Mallnock West. The temperatures confirm that regional metamorphism reached transitional sub-greenschist to lower greenschist facies conditions in the study area (ESM 1b).

Discussion

Polyphase ore formation

Textural observations indicate that the mineralization at Mallnock is polyphase. The scheelite-only mineralization at Mallnock West is represented by Scheelite 1 and consists of two subtypes (Scheelite 1a and Scheelite 1b). The early (“primary”) type Scheelite 1a exhibits relict zoning patterns and was affected by subsequent coupled dissolution-reprecipitation processes (Putnis 2002) with (re)crystallization of Scheelite 1a to the younger type Scheelite 1b (stages 1–2, Fig. 9a–b).

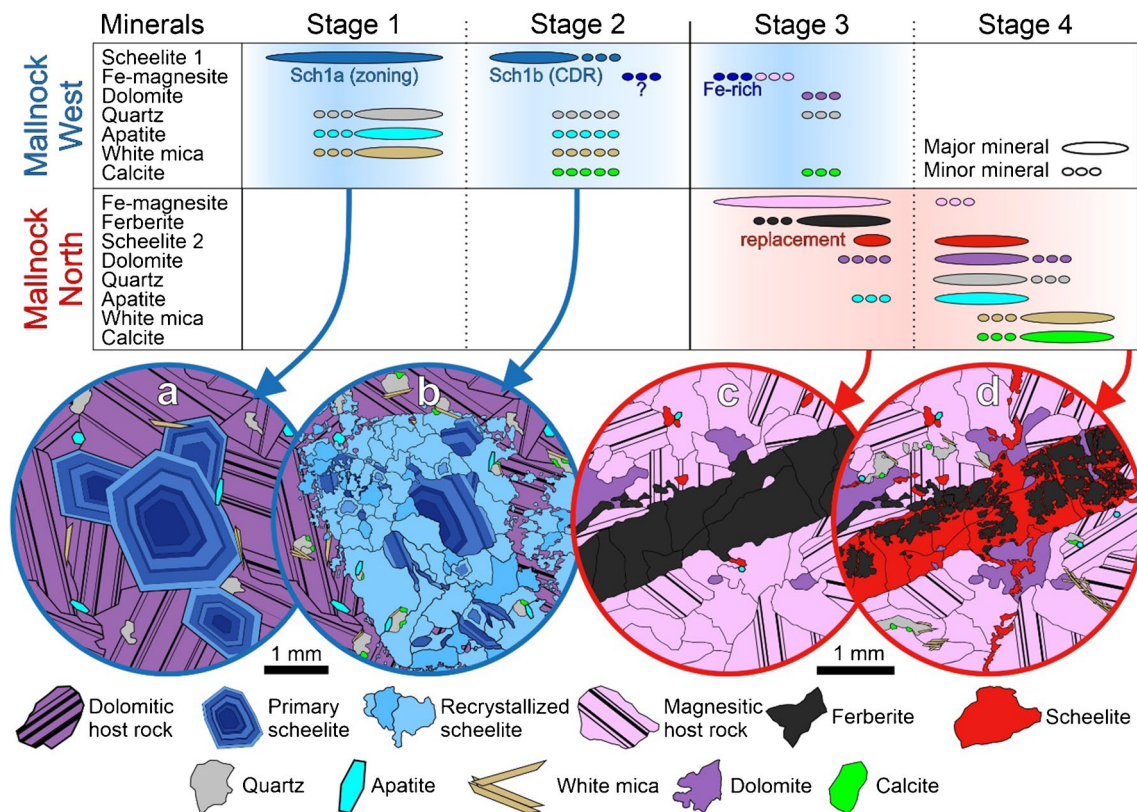


Fig. 9 Paragenetic sequence of the Mallnock mineralization and schematic sketches of the different mineralization stages at Mallnock West (**a, b**) and Mallnock North (**c, d**). **a** Formation of primary zoned early scheelite (Sch1a, blue) in dolomitic host rock at Mallnock West. **b** Subsequent coupled dissolution-precipitation (CDR) of Sch1a caus-

ing recrystallized scheelite (Sch1b, light blue). **c** Formation of ferberite veinlets (black) in Fe-magnesite at Mallnock North. **d** Late-stage replacement of ferberite by scheelite (Sch2, red) and coprecipitation of dolomite. For details see text

The zoning preserved in Scheelite 1a is interpreted as remnants of primary growth zonation. Such zoning patterns arise in minerals through cyclic, small-scale fluctuations in the chemical composition of melts or fluids during crystallization and have been documented in scheelite (Kwak and Tan 1981; Shore and Fowler 1996). Oscillatory zoning in scheelite is common in intrusion-related ore deposits such as in porphyry, skarn, and greisen systems but was also observed in scheelite from orogenic gold deposits (Brugger et al. 2000; Poulin et al. 2016; Sciuba et al. 2020; Miranda et al. 2022). In contrast, metamorphic remobilization of scheelite usually results in homogeneous textures as documented in the metamorphosed Felbertal scheelite deposit (Raith and Stein 2006; Kozlik et al. 2016).

At Mallnock North, the textural relationship between the host rocks (Fe-magnesite and dolomite), ferberite, and Scheelite 2 records a more complex history of consecutive hydrothermal/metamorphogenic(?) mineralization. Field observations at the magnesite-dolomite contacts confirm metasomatic replacement of the dolomitic host rocks by magnesite (Stage 3, Fig. 9c). Such metasomatic features

were documented in many other sparry magnesite deposits in the Eastern Alps and used as a key argument for the epigenetic metasomatic model of magnesite formation (e.g., Pohl 1990).

The fact that stockwork-like veinlets and patches with ferberite are exclusively found in Fe-magnesite indicates that their formation must be genetically linked (Stage 3, Fig. 9c). Because Scheelite 2 is replacing ferberite, the scheelite must be younger and postdates ferberite (Stage 4, Fig. 9d). Also, Scheelite 2 was not affected by coupled dissolution-precipitation processes as observed in Scheelite 1 (Fig. 5a–b). These textural relationships suggest that formation of Fe-magnesite, ferberite, and the subsequent replacement of the latter by Scheelite 2 postdate the formation of Scheelite 1. This interpretation is also confirmed by the geochronological data (see results above).

The precipitation of wolframite-group minerals and scheelite is strongly controlled by a decrease in temperature but also by increasing pH (e.g., due to the reaction of the fluid with carbonates) or decreasing salinity (Liu et al. 2021). Experimental and empirical studies show that neutral to

slightly acidic ($4 < \text{pH} < 6$) and relatively oxidized (between quartz-fayalite-magnetite and hematite-magnetite buffers) hydrothermal fluids favor the transport of tungsten (Wood and Samson 2000). At moderate temperatures (ca. 300 °C), tungsten is transported as oxy-anion complexes (e.g., WO_4^{2-}) and the reaction with Fe^{2+} and Mn^{2+} leads to the precipitation of wolframite only under reducing conditions (i.e., below the hematite-magnetite buffer; Wood and Samson 2000; Wang et al. 2020). The iron needed for this reaction is derived from the alteration of Fe-bearing minerals in the host rocks (e.g., Fe-chlorite, Lecumberri-Sanchez et al. 2017).

It is assumed that interaction with Fe-rich host rocks (in this case Fe-magnesite) was the source of Fe to form ferberite at Mallnock North. The relatively high Mg contents of ferberite support this interpretation (Fig. 6c). A two-step hydrothermal process is proposed, with the first step being the crystallization of Fe-magnesite, which increased the Ca/Mg and Ca/Fe ratio of the gradually cooling fluid. This was likely followed by the late-stage formation of a younger generation of dolomite (“Rosszahndolomit”), which is typical in sparry magnesite deposits (Pohl 1990; Henjes-Kunst et al. 2014). This late dolomite is commonly associated with ferberite and Scheelite 2 and therefore indicates the second step of a later paragenetic assemblage (stages 3–4, Fig. 9c–d).

Reaction of the tungsten mineralizing fluid with Fe-magnesite initially promoted the precipitation of ferberite causing an increase in the Ca/Fe ratio of the hydrothermal system (Stage 3, Fig. 9c; Neinavaie et al. 1989). Eventually, this change of physicochemical conditions favored scheelite stability and led to the replacement/overgrowth of ferberite by Scheelite 2 (stages 3–4, Fig. 9c–d). Thermodynamic modeling confirmed that scheelite has a higher solubility than ferberite in hydrothermal solutions (chemical system, W-Ca-Fe-Na-Cl-O-H; 300–400 °C, 50–150 MPa, and 1–3 mol/kg NaCl; Liu et al. 2021). Consequently, scheelite can replace ferberite over a wide range of temperatures and pressures. Thus, the well-documented textures of Scheelite 2 replacing and overgrowing ferberite (Figs. 4b, d–e, and 5c) do not necessarily represent a later separate mineralization phase but can also be understood as the final stage of a continuous mineralization process caused by either (i) the cooling of the hydrothermal fluid and an increase in molar Ca/Fe ratio (introduction of Ca or removal of Fe necessary) or (ii) decrease of the fluid pressure at constant Ca/Fe ratio (see Liu et al. 2021).

Ore-forming processes revealed by mineral chemistry

Substitution mechanisms

The general formula of the two tungstates scheelite and ferberite can be written as $\text{A}^{2+}\text{B}^{6+}\text{O}_4$; A = Ca, Fe, Mn, and

Table 2 Substitution mechanisms for scheelite (e.g., Nassau and Loiacono 1963; Ghaderi et al. 1999) and wolframite (e.g., Tindle and Webb 1989). A and B represent the two structural sites in scheelite and wolframite (ABO_4 ; A = Ca, Fe, Mn, and B = W). M^{3+} are trivalent cations (e.g., Fe, Sc, V, In, REE) substituting in wolframite

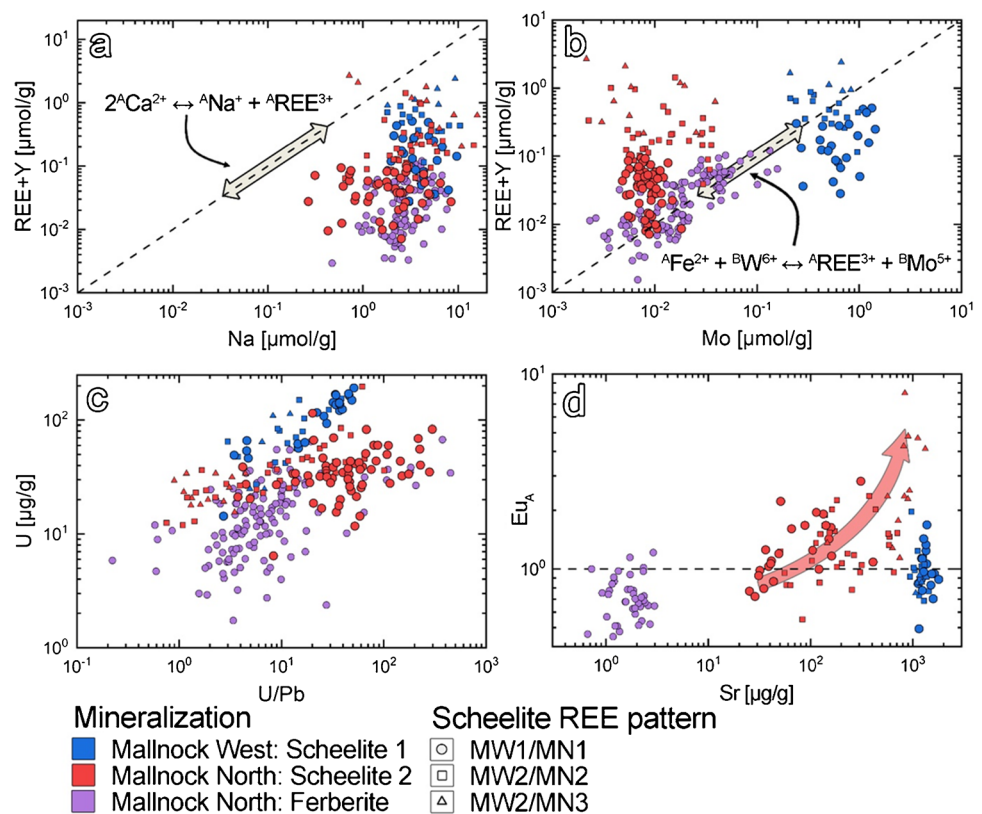
Scheelite		
S1	$2^{\text{A}}\text{Ca}^{2+}$	$\leftrightarrow \text{A}^{\text{Na}^+} + \text{A}^{\text{REE}^{3+}}$
S2	$\text{A}^{\text{Ca}^{2+}} + \text{B}^{\text{W}^{6+}}$	$\leftrightarrow \text{A}^{\text{REE}^{3+}} + \text{B}^{\text{(Nb,Ta)}^{5+}}$
S3	$3^{\text{A}}\text{Ca}^{2+}$	$\leftrightarrow 2^{\text{A}}\text{REE}^{3+} + \text{A}^{\square}$ (\square is a site vacancy)
Wolframite group		
W1	$\text{A}^{\text{(Fe,Mn)}^{2+}} + \text{B}^{\text{W}^{6+}}$	$\leftrightarrow \text{A}^{\text{M}^{3+}} + \text{B}^{\text{(Nb,Ta)}^{5+}}$
W2	$\text{A}^{\text{(Fe,Mn)}^{2+}} + \text{B}^{\square} + 3^{\text{B}}\text{W}^{6+}$	$\leftrightarrow \text{A}^{\square} + 4^{\text{B}}\text{(Nb,Ta)}^{5+}$
W3	$2^{\text{A}}\text{(Fe,Mn)}^{2+} + \text{B}^{\text{W}^{6+}}$	$\leftrightarrow 2^{\text{A}}\text{M}^{3+} + \text{B}^{\text{(Ti,Sn)}^{4+}}$

B = W. If the radius of the A cation is larger than 0.9 Å (e.g., Ca, Ba, Pb, Sr), these tungstates crystallize in the tetragonal scheelite ($^{[8]}\text{A}^{[4]}\text{WO}_4$) structure. If the radius of the A cation is below 0.9 Å (e.g., Fe, Mn, Co, Ni, Zn, Mg), they crystallize in the monoclinic wolframite ($^{[6]}\text{A}^{[6]}\text{WO}_4$) structure (Hazen et al. 1985; Macavei and Schulz 1993). Divalent cations with suitable ionic radii can be readily substituted for Ca ($^{[8]}\text{rCa}^{2+} = 1.12$ Å) in scheelite (e.g., $^{[8]}\text{rSr}^{2+} = 1.16$ Å, $^{[8]}\text{rPb}^{2+} = 1.29$ Å, $^{[8]}\text{rMn}^{2+} = 0.96$ Å) or Fe ($^{[6]}\text{rFe}^{2+} = 0.78$ Å) and Mn ($^{[6]}\text{rMn}^{2+} = 0.83$ Å) in wolframite (e.g., $^{[6]}\text{rMg}^{2+} = 0.72$ Å, $^{[6]}\text{rZn}^{2+} = 0.74$ Å, $^{[6]}\text{rCo}^{2+} = 0.745$ Å) by simple substitution (all ionic radii are taken from Shannon 1976).

Tungsten is present in the hexavalent state in both minerals and tetrahedrally coordinated ($^{[4]}\text{rW}^{6+} = 0.42$ Å) in scheelite and octahedrally coordinated ($^{[6]}\text{rW}^{6+} = 0.6$ Å) in wolframite. Commonly, tungsten is substituted by high field strength elements, such as Mo, Nb, or Ta. Molybdenum readily substitutes tungsten in scheelite ($^{[4]}\text{rMo}^{6+} = 0.41$ Å) forming a solid solution series with powellite (CaMoO_4). Interestingly, Mo rarely substitutes W in wolframite ($^{[6]}\text{rMo}^{6+} = 0.59$ Å), according to existing data. The pentavalent cations Nb and Ta are preferably incorporated into wolframite ($^{[6]}\text{rNb}^{5+}, \text{Ta}^{5+} = 0.64$ Å) and, to a limited extent, in scheelite ($^{[4]}\text{rNb}^{5+}, \text{Ta}^{5+} = 0.48$ Å).

The substitution of trivalent REE for Ca^{2+} and Fe^{2+} in scheelite and wolframite, respectively, requires a charge-balance mechanism enabled by coupled substitutions. The most common substitutions are summarized in Table 2. The same is true for tetravalent cations with small ionic radii (e.g., Ti^{4+} , Sn^{4+}), which are often substituted together with trivalent cations for tungsten into the wolframite structure. With regard to the REE, scheelite preferentially incorporates LREE (La–Nd) over HREE (Ho–Lu; $^{[8]}\text{rCa}^{2+}$ compared to $^{[8]}\text{rLa}^{3+} = 1.16$ Å and $^{[8]}\text{rLu}^{3+} = 0.98$ Å; e.g., Poulin et al. 2018), whereas wolframite rather fractionates

Fig. 10 Binary plots of trace elements in scheelite and ferberite from Mallnock. **a** Na vs. REE + Y plot showing an excess in Na in respect to the coupled substitution mechanism S1 (dashed line). **b** The positive correlation of Mo and REE + Y in ferberite ($r=0.7$) indicates a coupled substitution of these elements. **c** U vs. U/Pb diagram showing positive correlations; the highest U contents are found in Sch1. **d** Sr vs. Eu anomaly (Eu_A) showing rather constant Sr values in Sch1 and ferberite. Sch2 shows larger variation and moderate correlation of the two parameters



the HREE ($^{16}rFe^{2+}$ compared to $^{16}rLa^{3+} = 1.032 \text{ \AA}$ and $^{16}rLu^{3+} = 0.861 \text{ \AA}$; e.g., Harlaux et al. 2018a).

A clear dominance of LREE over MREE and HREE is only observed in one REE pattern of Scheelite 1 (subtype MW1). Most other REE pattern subtypes of Scheelite 1 show lower chondrite-normalized values of LREE and HREE compared to MREE and exhibit convex shapes (MW2-MW3, Fig. 7a–c). REE patterns of Scheelite 1 are significantly flatter than the sinistral inclined patterns of Scheelite 2 (MN1-MN3, Fig. 7d–f). Ferberite is characterized by low LREE values and similar bell-shaped patterns as REE patterns MN1 and MN2 of Scheelite 2 (Fig. 7d–e), suggesting that the bell-shaped patterns persist through the paragenetic sequence. Hence, the REE distribution of Scheelite 2 is inherited from ferberite from an early replacement process on and evolves towards higher ΣREE with distinct positive Eu anomalies in REE patterns MN3 (Figs. 7f and 10d).

The contents of Nb and Ta are low at Mallnock and no correlation between Nb + Ta and REE is seen for scheelite or ferberite, excluding the S2 and W1 substitution schemes (Table 2). Niobium and Ta can reach values in excess of 1000 μg/g particularly in high-temperature tungsten deposits associated with F-rich (peri-) granitic and greisen systems (Tindle and Webb 1989; Goldmann 2016; Harlaux et al. 2018a; Poulin et al. 2018; Sciuba et al. 2020; Miranda et al. 2022). The mobility of Nb and Ta depends on the concentration of complexing agents (e.g., F, Cl) in aqueous fluids

and is comparatively lower in low-temperature hydrothermal systems (e.g., in fluids of low-grade metamorphic origin; Tanis et al. 2015; Ague 2017). Accordingly, the low contents of Nb in scheelite ($\leq 0.8 \text{ μg/g}$) and ferberite ($\leq 1.6 \text{ μg/g}$) and especially of Ta (most analyses $< 1 \times 10^{-2} \text{ μg/g}$) at Mallnock disfavor the crystallization from a F-rich fluid of a high-temperature magmatic-hydrothermal system (Fig. 6c, ESM 3b).

The Na versus REE + Y plot shows that there is a considerable excess of Na in scheelite and ferberite but without any correlation with the REE (Fig. 10a). Sodium could therefore be involved in the substitution but not via the coupled S1 scheme (Table 2) and a more complex coupled substitution mechanism must take effect. Incorporation of trivalent REE by the substitution of the A^{2+} cation (S3, Table 2) causes a site vacancy expanding the crystal structure which could enable substitution of larger cations like Na^+ (Wang et al. 2022). The (moderate) correlation of Na with divalent trace elements at Mallnock North (i.e., scheelite = Sr, Ba, Pb [$r \approx 0.6$], see Pearson correlation in ESM 3c) could point to such a substitution mechanism. In this case, Na^+ as a charge-balancing element (comparable to Li^+ ; Harlaux et al. 2018a) would be incorporated into the vacancies of the A position in the crystal lattice. The higher Na contents in scheelite also indicate a fluid with increased Na activity.

The positive correlation of Mo and REE + Y ($r=0.7$) in ferberite indicates a coupling between these elements that can be described by a modified coupled W1 scheme

(Table 2, Fig. 10b) via the exchange of ${}^A\text{Fe}^{2+} + {}^B\text{W}^{6+} \leftrightarrow {}^A\text{REE}^{3+} + {}^B\text{Mo}^{5+}$ (Zhao et al. 2018). This appears to be an effective mechanism to incorporate Mo at Mallnock since the contents are mostly above the global mean (Fig. 6c). For scheelite, however, no such correlation exists and data from Mallnock West and North are clearly separated in this plot. A possible explanation is that Scheelite 1 reflects the Mo content of the host rock, whereas Scheelite 2 inherited its Mo content as a result of ferberite replacement.

Incorporation of U in tungstates

Scheelite from Mallnock is particularly enriched in U (6.4–200 $\mu\text{g/g}$) with Scheelite 1 having the highest U contents (Fig. 10c). It is unclear how and in which valence state U is incorporated in the crystal structure of ferberite and scheelite. Due to the considerable differences in ionic sizes between U (${}^{161}\text{rU}^{6+/4+} = 0.73/0.89 \text{ \AA}$; ${}^{141}\text{rU}^{6+} = 0.52 \text{ \AA}$) and W amounting to 22–48% in wolframite and 24% in scheelite, respectively, an isovalent substitution should be limited from crystal chemical considerations. Other coupled substitutions proposed to explain the incorporation of U in wolframite are ${}^A(\text{Fe,Mn})^{2+} + 2{}^B\text{W}^{6+} \leftrightarrow {}^A\text{U}^{4+} + 2{}^B\text{Mo}^{5+}$ and $2{}^A(\text{Fe,Mn})^{2+} + {}^B\text{W}^{6+} \leftrightarrow 2{}^A\text{REE}^{3+} + {}^B\text{U}^{4+}$ (e.g., Tindle and Webb 1989). It was also suggested that U can replace Fe and Mn (size difference of 3–14%) in the octahedral site regardless of its oxidation state (Lüders et al. 2009). Moreover, uranium may also be incorporated as uranyl ion (UO_2^{2+}) replacing Fe and Mn in wolframite (Swart and Moore 1982), a scheme that should also consider increasing oxygen fugacity during the final phase of ferberite crystallization. Substitution of U (${}^{181}\text{rU}^{6+/4+} = 0.86/1.0 \text{ \AA}$) for Ca in scheelite is a possible but less likely mechanism because of the size difference (10–23%). The incorporation of uranyl ions in scheelite seems rather unlikely as studies on natural calcite showed that UO_2^{2+} is mainly incorporated in sixfold coordination (Kelly et al. 2003).

Effect of trace elements on cathodoluminescence

Cathodoluminescence has been successfully used to document micro-textures of scheelite (Brugger et al. 2000; Raith and Stein 2006; Poulin et al. 2016). Intrinsic (self-luminescence band related to the WO_4^{2-} group) and extrinsic (impurities) mechanisms determine the luminescence of scheelite. Several trace elements (e.g., Mo, REE, Nb, Ta, and U) may have a significant influence on the CL signal of scheelite (Götze et al. 2001). As described above, CL textures of Scheelite 1 are complex and reveal relict growth zoning in its cores (Fig. 5a–b) suggesting that the primary zonation was partially overprinted by hydrothermal alteration. In contrast, Scheelite 2 exhibits homogeneous CL textures and no recrystallization (Fig. 5c).

There is no clear correlation of CL intensity and the REE patterns (Fig. 5a). However, in many cases, higher ΣREE contents are measured in the bright CL domains of Scheelite 1b where particularly the MREE become enriched (i.e., REE pattern MW2, Fig. 5b). The zoned and CL dark Scheelite 1a often has higher U and Mo contents, while the surrounding fine-grained Scheelite 1b with brighter CL has lower contents of these elements (Fig. 5a–b). Thus, the decrease of U and Mo related to the fluid-mediated dissolution-reprecipitation of Scheelite 1 enhanced CL brightness in Scheelite 1b compared to Scheelite 1a.

Molybdenum is known to control the luminescence in scheelite (Brugger et al. 2000; Poulin et al. 2016), but at Mallnock, the Mo contents of scheelite are generally low causing its blue UV fluorescence (Fig. 3c, e–f). Hence, it is likely that at Mallnock U is the main element controlling the CL intensity. Scheelite crystallization under relatively oxidizing conditions favors incorporation of ${}^{141}\text{U}^{6+}$ (and ${}^{141}\text{Mo}^{6+}$) for ${}^{141}\text{W}^{6+}$ resulting in weakened CL intensity. A similar correlation of U and lower CL intensity was also found in the Daboashan porphyry Mo–W deposit in South China (Su et al. 2019) and the Cantung skarn deposit in Canada (Miranda et al. 2022).

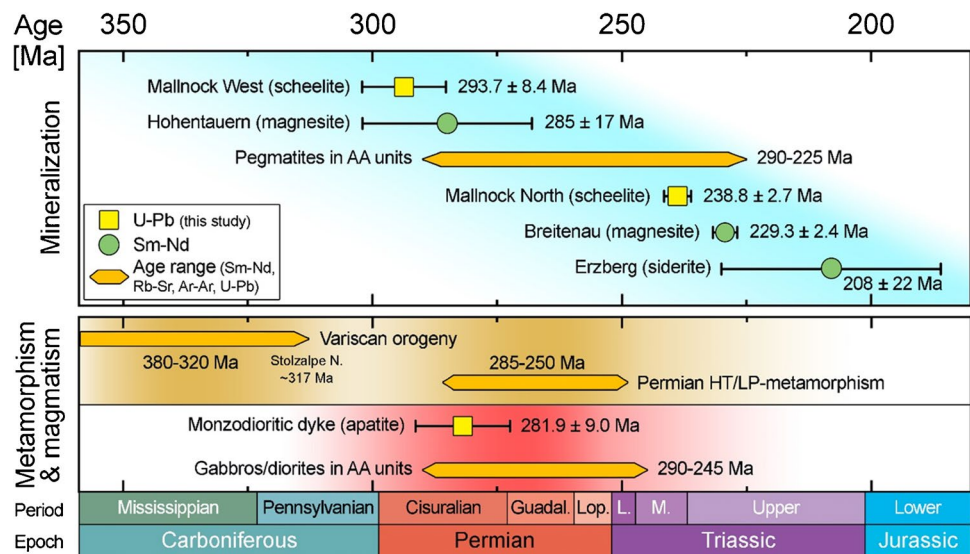
Strontium shows the opposite trend to U. Domains richer in Sr are lower in U and CL-brighter (Fig. 5a–b). Subtype Scheelite 1b formed by coupled dissolution-reprecipitation processes and has taken up more Sr, likely from the adjacent metamorphic host rocks. Such a process was discussed for metamorphic remobilized scheelite at the Felbertal and Tux-Lanersbach deposits (Raith et al. 1995; Kozlik et al. 2016). At Mallnock North, Sr and U seem to have been simultaneously incorporated in Scheelite 2 (Fig. 5c) and were inherited during ferberite replacement (Fig. 10c–d). The increase of Sr related to REE patterns MN1 to MN3 could be ascribed to the Sr release during continued alteration of Fe-magnesite to late dolomite (Fig. 10d).

Geodynamics and genetic considerations

Combining the data from this study with available geological/geodynamic information helps constrain the genesis of this unusual tungsten-magnesite mineralization. The U–Pb scheelite dating yielded early Permian ($294 \pm 8 \text{ Ma}$, Scheelite 1–Mallnock West) and Middle Triassic ($239 \pm 3 \text{ Ma}$, Scheelite 2–Mallnock North) dates. It is the first recognition of a “Permian/Triassic” event in the Gurktal Alps which are part of the Drauzug-Gurktal Nappe System. The new dates link the tungsten mineralization at Mallnock to geodynamic and metallogenetic processes in the Eastern Alps in this period (Fig. 11).

From the Permian to the Middle Triassic, the Paleozoic metasediments of the Drauzug-Gurktal Nappe System were part of the Adriatic plate located at the northern margin of

Fig. 11 Timeline with age data compilation of this study (Mallnock West-Scheelite 1, Mallnock North-Scheelite 2) and other mineralizing and geologic events in the Austroalpine (AA) units in the Eastern Alps. Note: Sm–Nd magnesite data are from Henjes-Kunst et al. (2014) and Azim Zadeh et al. (2015); Sm–Nd siderite data are from Prochaska and Henjes-Kunst (2009); age ranges of pegmatites are taken from Schuster and Stüwe (2008), Kroner and Romer (2013) and references therein. Guadal. = Guadalupian, Lop. = Lopingian, L. = Lower, M. = Middle



the Meliata-Hallstatt ocean basin (westernmost segment of the Paleotethys; Kozur 1991; Schmid et al. 2004). The geodynamic evolution of this crustal segment is characterized by late Paleozoic (post-Variscan) extension followed by large-scale rifting during the Permian and Triassic (Neubauer et al. 2022). The associated igneous and metamorphic activity reflects the breakup of Pangea that eventually led to the opening of the Meliata-Hallstatt ocean (Neubauer et al. 2000; Schuster and Stüwe 2008). Crustal extension was accompanied by underplating of the lower crust by mantle-derived melts between 290 and 245 Ma (e.g., Zanetti et al. 2013). The timing of low-pressure high-temperature metamorphism in various Austroalpine basement units range from ca. 285 to 250 Ma (Schuster and Stüwe 2008 and references therein). This Permian metamorphism was a consequence of lithospheric thinning, which included mantle upwelling and partial melting in the lower/middle crust and also caused increased heat flow in the overlying upper crustal units (Leitner et al. 2013). Lithium (spodumene) pegmatites as well as barren ones formed by the anatexis of crustal rocks and differentiation of these melts (Knoll et al. 2023) between 290 and 225 Ma (Fig. 11).

The new dates of scheelite from Mallnock broadly coincide with magmatic and metamorphic/anatectic processes in the middle to lower crust in the former Adriatic plate during the Permian to Triassic. We envisage that ore formation at Mallnock was triggered by enhanced fluid circulation due to elevated geothermal gradients in the crust. Age data from various hydrothermal ore deposits across Western and Central Europe as well as from North Africa demonstrate that the spatial distribution and temporal emplacement of these deposits can be linked with the breakup of Pangea (Burisch et al. 2022). The conceptual model of rift-related hydrothermal vein and stratabound mineralization includes episodic

mixing of basement-derived metal-enriched hydrothermal fluids and sediment-derived brines (Fusswinkel et al. 2013). These processes are controlled essentially by mid-crustal fluids released in response to heating and decompression related to crustal thinning and exhumation (Staude et al. 2009).

In the study area, the emplacement of a monzodioritic dike (282 ± 9 Ma) overlaps within the uncertainties with the U–Pb date of 294 ± 8 Ma determined for Scheelite 1 (Fig. 11). Since the next gabbroic diorite occurs about 500 m west of the tungsten mineralization (Fig. 2) and no dike rocks were intersected in the exploration drillings (Fig. 3a), a causal genetic relation between these two events seems unlikely. Nevertheless, the emplacement of these dikes supports the concept of extension-related early Permian magmatism in the Stolzalpe Nappe. Deposition of thick siliciclastic successions (e.g., conglomerates) representing graben fillings on the top of the Stolzalpe Nappe are also consistent with Permian rifting in this region (Sylvester 1989).

The U–Pb date of texturally complex Scheelite 1 has a rather large uncertainty of ± 8 Ma so is discussed here in more detail. Micro-textures of Scheelite 1 document an early subtype (Sch1a), which was affected by coupled dissolution-reprecipitation and recrystallization (Sch1b, Fig. 5a–b). The size of the laser spot ($80 \mu\text{m}$) did not allow definite resolution of coarser scheelite domains of Scheelite 1a from the fine-crystalline Scheelite 1b, as a large-as-possible spot size increases the volume analyzed while simultaneously minimizing downhole elemental fractionation errors (Wintzer et al. 2022). Thus, it is possible that the age of 294 ± 8 Ma represents a combination of the two distinct scheelite textures Scheelite 1a and Scheelite 1b with slightly different dates, which cannot be reliably separated. Guided by CL imaging done after the LA-ICP-MS analyses, the Scheelite

1 U–Pb data were therefore carefully re-evaluated and show hints to the presence of two populations. Domains of Scheelite 1a (zoning, CL-darker) yielded an isochron date of 309 ± 12 Ma ($n=9$; see ESM 2b and 4a), whereas the reprecipitated domains of Scheelite 1b (CL-brighter) yielded a date of 286 ± 11 Ma ($n=13$).

Interestingly, an $^{40}\text{Ar}/^{39}\text{Ar}$ white mica cooling age of 316 ± 3 Ma was determined in an impure calcitic marble that is located 1 km to the east of the tungsten mineralization (Iglseider et al. 2016). The Ordovician to Devonian volcano-sedimentary rocks of the Stolzalpe Nappe were metamorphosed at maximum temperatures of 300–320 °C (Rantitsch et al. 2020) that is confirmed by the RSCM temperature of 296 ± 27 °C obtained from Mallnock West. Hence, low grade regional metamorphism in the Stolzalpe Nappe likely is of Variscan age.

One (alternative) interpretation for Mallnock West could be that Scheelite 1a was formed during the late Variscan metamorphism and was subsequently remobilized during a first phase in the Permian causing subtype Scheelite 1b. However, we are aware that the number of analyses and the uncertainties are insufficient to confirm two distinct separated mineralization stages at Mallnock West. The meaningfulness of the 294 ± 8 Ma date obtained from the complete data set ($n=30$) remains intact. In respect of the two ore zones at Mallnock West and Mallnock North, the two dates do not overlap in uncertainty (Sch1: 294 ± 8 Ma and Sch2: 239 ± 3 Ma). Thus, scheelite formation in the two ore zones is clearly separated in time. This interpretation is also consistent with geological and textural observations. Therefore, scheelite-only mineralization at Mallnock West formed before the Fe-magnesite-ferberite-scheelite mineralization at Mallnock North (Fig. 11). The 239 ± 3 Ma date for Scheelite 2 from Mallnock North is geochronologically well constrained ($n=30$, low uncertainty) and Scheelite 2 does not show any evidence of subsequent recrystallization. Hence, we are confident that this date is not affected by subsequent resetting of the U–Pb system, what has been noted as a problem in some studies of wolframite (Harlaux et al. 2018b; Carr et al. 2021).

Polyphase hydrothermal tungsten mineralization at Mallnock is geotectonically linked with prolonged Permian–Triassic extension tectonics related to the breakup of Pangea. It formed during multiple hydrothermal events over a time period of about 50 million years. The Permian (ca. 290 Ma) date of Scheelite 1 is younger than the Silurian to Devonian stratigraphic age of the carbonate host rocks (Höll 1970). It reflects an initial tungsten mineralizing phase related to crustal fluid circulation at the beginning of the breakup of Pangea during the early Permian. At a later stage, the dolomitic host rocks at Mallnock North were infiltrated by Mg- (Fe–Mn) and W-bearing hydrothermal fluids, leading first to the formation of Fe-magnesite and subsequently ferberite.

The subsequent transition of ferberite to Scheelite 2 is dated at 239 ± 3 Ma and provides the younger time bracket of the hydrothermal activity during the Middle Triassic (Fig. 11).

This stratabound carbonate-hosted style of tungsten mineralization shows a completely different chemical signature compared to granite-related tungsten deposits (Goldmann 2016; Harlaux et al. 2018a; Poulin et al. 2018; Miranda et al. 2022). Irrespective of slight differences, scheelite and ferberite from Mallnock West and Mallnock North generally have noticeably lower Mo, Nb, and Ta contents than those from granite-related tungsten deposits of magmatic-hydrothermal origin (Table 1, Fig. 6c). Similar low contents of Nb (and Ta) in scheelite from orogenic vein-type mineralization in the Otago Schist (New Zealand) were interpreted as the result of the interaction of fluids of orogenic provenance with the metasedimentary host rocks (Palmer et al. 2022). The clear chemical differences between ferberite/scheelite of the carbonate-hosted tungsten mineralization at Mallnock and wolframite/scheelite deposits related to magmatic-hydrothermal processes (Goldmann et al. 2013; Harlaux et al. 2018a; Poulin et al. 2018; Miranda et al. 2022) can be potentially ascribed to different types of tungsten deposits.

Metallogenic context

As magnesite is the main host rock of tungsten mineralization at Mallnock North, it is reasonable to refer to possible links with magnesite deposits in the Eastern Alps. These magnesite deposits are primarily of the sparry type (“Veitsch type”) and hosted in early to late Paleozoic shallow marine carbonate metasediments (see Pohl 1990 and references therein). It is widely accepted that magnesium metasomatism played a key role in their formation, although the timing and hence the genesis are still debated (see Prochaska 2016 and references therein).

The oxygen isotope compositions of sparry magnesites are quite variable and correlate with the degree of metamorphism of the host rocks (Kralik et al. 1989). The stable isotope composition of magnesite from Mallnock (Raith et al. 1988) is comparable with that of other sparry magnesite deposits in the Eastern Alps (Breitenau, Henjes-Kunst et al. 2014; Hohentauern, Azim Zadeh et al. 2015) and the Tux-Lanersbach magnesite-scheelite deposit (Raith et al. 1995). This accordance of the data suggests a genetic relationship of all these deposits including Mallnock.

Fluid inclusion studies in magnesite and scheelite associated with magnesite indicate minimum formation temperatures in a range of 230–290 °C and moderate to higher salinity (10–20 mass% NaCl equiv.) H_2O -NaCl-(CaCl_2 - MgCl_2) fluids (Raith et al. 1995; Azim Zadeh et al. 2015). Crush-leach analyses of fluid inclusions of sparry magnesite from the Eastern Alps indicate an origin of the fluid from extremely evaporated seawater (Prochaska 1997). Based

on Sm–Nd dating of magnesite, a Middle Triassic age was reported for Breitenau deposit (229.3 ± 2.4 Ma; Henjes-Kunst et al. 2014) and a late Carboniferous to early Permian age for Hohentauern (model 1, 285 ± 17 Ma; Azim Zadeh et al. 2015; Fig. 11).

Numerous siderite deposits are also found in Austroalpine Paleozoic geological units, including Austria's largest Fe deposit at Erzberg for which an Upper Triassic date was published (208 ± 22 Ma, siderite Sm–Nd isochron; Prochaska and Henjes-Kunst 2009). It is beyond the scope of this paper to discuss the metallogeny of the Eastern Alps, but it is pointed out that the scheelite ages for Mallnock add important new data for deciphering this Permian–Triassic metallogenetic epoch in the Eastern Alps (Fig. 11).

Where does the tungsten come from?

Enrichment of tungsten by volcanism and sedimentary-exhalative processes was favored in early genetic models of scheelite deposits in the Eastern Alps (Maucher 1965; Höll et al. 1972). Following this model, a volcanic pre-concentration of tungsten in dolomitic rocks was discussed for Mallnock with extensive subsequent mobilization (Neinavaie et al. 1989). Alternatively, a pre-enrichment in sediments containing abundant carbonaceous material is also possible. Graphitic schists in contact with the scheelite/ferberite-bearing carbonate rocks at Mallnock have higher W contents ($25 \mu\text{g/g}$) than those in the vicinity of barren carbonates ($5 \mu\text{g/g}$; Neinavaie et al. 1989). An interesting model is presented by Romer and Kroner (2016), in which a chemical-sedimentary pre-enrichment of W and Sn in the peri-Gondwana realm is thought to be the prerequisite for the later formation of magmatic-hydrothermal tungsten-tin deposits in distinct belts. In the case of Mallnock, a similar origin of the tungsten pre-enrichment in graphitic schists can be postulated. Permian–Triassic rift-related, hydrothermal processes may have led to the subsequent mobilization of tungsten, whereas scheelite or ferberite were only able to form if sufficient tungsten was locally available.

Conclusions

The stratabound carbonate-hosted ferberite-scheelite mineralization at Mallnock is associated with Fe-magnesite and represents a peculiar type of tungsten mineralization in the Eastern Alps. Micro-textural (CL) and trace element chemical analyses (LA-ICP-MS) of scheelite and ferberite combined with U–Pb dating of scheelite confirm a polyphase development of tungsten mineralization.

Scheelite and ferberite at Mallnock are characterized by higher contents of Na, Sr, and particularly U, whereas

Mo, Nb, Ta, and the REE are notably depleted compared to global tungsten deposits of granitic/pegmatitic origin. Hence, the non-granitic origin of the Mallnock mineralization as evidenced by the geology is also supported by the distinct chemical differences to granite-related magmatic-hydrothermal tungsten deposits.

Scheelite 1 in dolomitic host rocks at Mallnock West is dated at 294 ± 8 Ma; i.e., early Permian. At Mallnock North, Scheelite 2 occurs in Fe-magnesite replacing ferberite. The well-constrained date of 239 ± 3 Ma for Scheelite 2 concludes the polyphase evolution of hydrothermal activity in the Middle Triassic. The Permian and Triassic scheelite dates link the genesis of the tungsten-magnesite mineralization at Mallnock to the overall breakup of Pangea. Crustal extension and thinning caused an increased heat flow and enhanced fluid circulation within the Austroalpine upper crust. The emplacement of a monzodioritic dike that was dated at 282 ± 9 Ma is also an expression of this extensional event though there is no apparent causal relationship to tungsten mineralization. Sedimentary-diagenetic or late Variscan orogenic fluids are possible candidates for leaching metals (Mg, Fe, W) from the basement/carbonaceous(?) sediments as they ascended. Upon interaction with dolomitic host rocks, they caused metasomatic magnesite formation followed by formation of ferberite and late stage scheelite. Our findings show that a modern metallogenetic model of tungsten mineralization in the Eastern Alps must also consider the larger scale Permian–Triassic geodynamics and possible links to magnesite-siderite mineralization in the Eastern Alps.

Supplementary information The online version contains supplementary material available at <https://doi.org/10.1007/s00126-024-01250-x>.

Acknowledgements We thank Maik Zimmermann for assistance with sample preparation, Federica Zaccharini for support at the EPMA (Montanuniversität Leoben), and Beate Schmitte for help with the LA-ICP-MS (University of Münster). Sincere thanks to Chao Zhang for her invaluable analytical work and data reduction at Washington State University. Gerd Rantitsch is thanked for RSCM measurements. Moreover, we thank Tanja Knoll for help during fieldwork and Hassan Neinavaie for providing data and sample material. Thanks to Benjamin Huet and Ralf Schuster for fruitful discussions and Magdalena Mandl, Daniela Gallhofer, and Etienne Skrzypek for support at the ICP-MS (University of Graz). Many thanks also to Julia Weilbold and Holger Paulick for their contribution to the project organization and comments on the manuscript. We are grateful to Associate Editor Matthieu Harlaux, Christopher Holm-Denoma, Lisard Torró, Editor-in-Chief Karen Kelley, and Heather L. Welch for their critical and constructive comments which significantly improved the manuscript. Any use of trade, firm, or product names is for descriptive purposes only and does not imply endorsement by the U.S. Government.

Author contribution Florian Altenberger and Johann G. Raith contributed to the study conception and design. Field work and sample collection were completed by Florian Altenberger, Johann G. Raith, and Christoph Iglseider. Material preparation, data collection, and analysis were performed by Florian Altenberger (sample preparation, EPMA,

LA-ICP-MS, MLA), Joachim Krause (EPMA, LA-ICP-MS), Niki E. Wintzer (U–Pb scheelite dating), Christoph Iglseider (U–Pb apatite dating, RSCM), Kai Bachmann (MLA), and Jasper Berndt (LA-ICP-MS). All authors contributed to the interpretation of the data. The manuscript was written by Florian Altenberger, Johann G. Raith, and Christoph Iglseider. Authors Joachim Krause, Niki E. Wintzer, Kai Bachmann, and Jasper Berndt commented on the previous versions of the manuscript and approved the final manuscript.

Funding Open access funding provided by Montanuniversität Leoben. This study received funding from the initiative “Research partnerships mineral raw materials (MRI—Forschungspartnerschaften Mineralrohstoffe)” of the Austrian Federal Ministry of Education, Science, and Research, a project scheme administrated by GeoSphere Austria.

Declarations

Conflict of interest The authors declare no competing interests.

Open Access This article is licensed under a Creative Commons Attribution 4.0 International License, which permits use, sharing, adaptation, distribution and reproduction in any medium or format, as long as you give appropriate credit to the original author(s) and the source, provide a link to the Creative Commons licence, and indicate if changes were made. The images or other third party material in this article are included in the article’s Creative Commons licence, unless indicated otherwise in a credit line to the material. If material is not included in the article’s Creative Commons licence and your intended use is not permitted by statutory regulation or exceeds the permitted use, you will need to obtain permission directly from the copyright holder. To view a copy of this licence, visit <http://creativecommons.org/licenses/by/4.0/>.

References

- Ague JJ (2017) Element mobility during regional metamorphism in crustal and subduction zone environments with a focus on the rare earth elements (REE). *Am Mineral* 102:1796–1821. <https://doi.org/10.2138/am-2017-6130>
- Altenberger F, Raith JG, Weilbold J, Auer C, Knoll T, Paulick H, Schedl A, Aupers K, Schmidt S, Neinavaie H (2021) Casting new light on tungsten deposits in the Eastern Alps. *J Appl Reg Geol* 172:63–72. <https://doi.org/10.1127/zdgg/2021/0262>
- Azim Zadeh A, Ebner F, Jiang S-Y (2015) Mineralogical, geochemical, fluid inclusion and isotope study of Hohentauern/Sunk sparry magnesite deposit (Eastern Alps/Austria): implications for a metasomatic genetic model. *Miner Petrol* 109:555–575. <https://doi.org/10.1007/s00710-015-0386-2>
- Bachmann K, Frenzel M, Krause J, Gutzmer J (2017) Advanced identification and quantification of in-bearing minerals by scanning electron microscope-based image analysis. *Microsc Microanal* 23:527–537. <https://doi.org/10.1017/S1431927617000460>
- BEV (2016) Karte 3106, Radenthein 1:50.000 (ÖK50-UTM, NL33-04-06 - Bad Kleinkirchheim, Turracherhöhe, Nockberge). Bundesamt für Eich- und Vermessungswesen (BEV), Wien
- Beysac O, Goffé B, Chopin C, Rouzaud JN (2002) Raman spectra of carbonaceous material in metasediments: a new geothermometer. *J Metamorph Geol* 20:859–871. <https://doi.org/10.1046/j.1525-1314.2002.00408.x>
- Briegleb D (1991) Ein epigenetisches Modell der Scheelitlagerstätte Felbertal (Land Salzburg). *Eur J Mineral* 3:43
- Brugger J, Bettioli AA, Costa S, Lahaye Y, Bateman R, Lambert DD, Jamieson DN (2000) Mapping REE distribution in scheelite using luminescence. *Mineral Mag* 64:891–903. <https://doi.org/10.1180/002646100549724>
- Burisch M, Markl G, Gutzmer J (2022) Breakup with benefits - hydrothermal mineral systems related to the disintegration of a supercontinent. *Earth Planet Sc Lett* 580:117373. <https://doi.org/10.1016/j.epsl.2022.117373>
- Carr PA, Mercadier J, Harlaux M, Romer RL, Moreira E, Legros H, Cuney M, Marignac C, Cauzid J, Salsi L, Lecomte A, Rouer O, Peiffert C (2021) U/Pb geochronology of wolframite by LA-ICP-MS; mineralogical constraints, analytical procedures, data interpretation, and comparison with ID-TIMS. *Chem Geol* 584:120511. <https://doi.org/10.1016/j.chemgeo.2021.120511>
- Cave B, Pitcairn I, Craw D, Large R, Thompson J, Johnson S (2017) A metamorphic mineral source for tungsten in the turbidite-hosted orogenic gold deposits of the Otago Schist, New Zealand. *Miner Deposita* 52:1–23. <https://doi.org/10.1007/s00126-016-0677-5>
- Chen G, Gao J-F, Lu J, Zhang R (2020) In situ LA-ICP-MS analyses of mica and wolframite from the Maoping tungsten deposit, southern Jiangxi, China. *Acta Geochim* 39:811–829. <https://doi.org/10.1007/s11631-020-00423-5>
- Chew DM, Petrus JA, Kamber BS (2014) U–Pb LA–ICPMS dating using accessory mineral standards with variable common Pb. *Chem Geol* 363:185–199. <https://doi.org/10.1016/j.chemgeo.2013.11.006>
- Deng X-D, Luo T, Li J-W, Hu Z-C (2019) Direct dating of hydrothermal tungsten mineralization using in situ wolframite U–Pb chronology by laser ablation ICP-MS. *Chem Geol* 515:94–104. <https://doi.org/10.1016/j.chemgeo.2019.04.005>
- Dostal J, Kontak D, Chatterjee AK (2009) Trace element geochemistry of scheelite and rutile from metatubidite-hosted quartz vein gold deposits, Meguma Terrane, Nova Scotia, Canada: genetic implications. *Miner Petrol* 97:95–109. <https://doi.org/10.1007/s00710-009-0067-0>
- Feitzinger G, Paar WH, Tarkian M, Reche R, Weinzierl O, Prochaska W, Holzer H (1995) Vein type Ag–(Au)–Pb, Zn, Cu–(W, Sn) mineralization in the Southern Kreuzeck Mountains, Carinthia Province, Austria. *Miner Petrol* 53:307–332. <https://doi.org/10.1007/BF01160154>
- Ferenc Š, Uher P (2007) Magnesian wolframite from hydrothermal quartz veins in the Rochovce granite exocontact, Ochtiná, Western Carpathians, Slovakia. *Neues Jb Miner Abh* 183:165–172. <https://doi.org/10.1127/0077-7757/2007/0066>
- Fritz A, Krainer K (2007) Vegetationsgeschichtliche und floristisch-stratigraphische Untersuchungen im Oberkarbon und Unterperm der Ost- und Südalpen (Teil 2). *Carinthia II* 117:91–148
- Fusswinkel T, Wagner T, Wälle M, Wenzel T, Heinrich CA, Markl G (2013) Fluid mixing forms basement-hosted Pb–Zn deposits: Insight from metal and halogen geochemistry of individual fluid inclusions. *Geology* 41:679–682. <https://doi.org/10.1130/G34092.1>
- Ghaderi M, Palin M, Campbell IH, Sylvester PJ (1999) Rare earth element systematics in scheelite from hydrothermal gold deposits in the Kalgoorlie–Norseman Region, Western Australia. *Econ Geol* 94:423–438. <https://doi.org/10.2113/gsecongeo.94.3.423>
- Giese U (1988) Lower Paleozoic volcanic evolution at the northwestern border of the Gurktal nappe, Upper Austroalpine, Eastern Alps. *Schweiz Miner Petrol Mitt* 68:381–396
- Goldmann S (2016) Mineralogical-geochemical characterisation of cassiterite and wolframite ores for an analytical fingerprint: focus on trace element analysis by LA-ICP-MS. Dissertation, Leibniz-Universität Hannover
- Goldmann S, Melcher F, Gäbler H-E, Dewaele S, Clercq FD, Muchez P (2013) Mineralogy and trace element chemistry of ferberite/

- reinite from tungsten deposits in Central Rwanda. *Minerals* 3:121–144. <https://doi.org/10.3390/min3020121>
- Götze J, Plötze M, Habermann D (2001) Origin, spectral characteristics and practical applications of the cathodoluminescence (CL) of quartz – a review. *Miner Petrol* 71:225–250. <https://doi.org/10.1007/s007100170040>
- Guillong M, Hametner K, Reusser E, Wilson SA, Günther D (2005) Preliminary characterisation of new glass reference materials (GSA-1G, GSC-1G, GSD-1G and GSE-1G) by laser ablation-inductively coupled plasma-mass spectrometry using 193 nm, 213 nm and 266 nm wavelengths. *Geostand Geoanal Res* 29:315–331. <https://doi.org/10.1111/j.1751-908X.2005.tb00903.x>
- Haditsch JG, Mostler H (1983) Zeitliche und stoffliche Gliederung der Erzvorkommen im Innsbrucker Quarzphyllit. *Geol-Palaeontol Mitt Inn* 12:1–40
- Harlaux M, Mercadier J, Marignac C, Peiffert C, Cloquet C, Cuney M (2018a) Tracing metal sources in peribatholithic hydrothermal W deposits based on the chemical composition of wolframite: the example of the Variscan French Massif Central. *Chem Geol* 479:58–85. <https://doi.org/10.1016/j.chemgeo.2017.12.029>
- Harlaux M, Romer RL, Mercadier J, Morlot C, Marignac C, Cuney M (2018b) 40 Ma of hydrothermal W mineralization during the Variscan orogenic evolution of the French Massif Central revealed by U-Pb dating of wolframite. *Miner Deposita* 53:1–51. <https://doi.org/10.1007/s00126-017-0742-8>
- Hazen RM, Finger LW, Mariathasan JWE (1985) High-pressure crystal chemistry of scheelite-type tungstates and molybdates. *J Phys Chem Solids* 46:253–263. [https://doi.org/10.1016/0022-3697\(85\)90039-3](https://doi.org/10.1016/0022-3697(85)90039-3)
- Henjes-Kunst F, Prochaska W, Niedermayr A, Sullivan N, Baxter E (2014) Sm–Nd dating of hydrothermal carbonate formation: an example from the Breitenau magnesite deposit (Styria, Austria). *Chem Geol* 387:184–201. <https://doi.org/10.1016/j.chemgeo.2014.07.025>
- Höll R (1970) Die Zinnober-Vorkommen im Gebiet der Turracher Höhe (Nock-Gebiet/Österreich) und das Alter der Eisenhut-Schieferserie. *Neues Jahrb Geol PM* 1970:201–224
- Höll R, Eichhorn R (1998) Tungsten mineralization and metamorphic remobilization in the Felbertal scheelite deposit, Central Alps, Austria. In: Vokes FM, Marshall B, Spry PG (eds) *Reviews in Economic Geology*. Society of Economic Geologists, Littleton, CO, USA, pp 233–264
- Höll R, Maucher A, Westenberger H (1972) Synsedimentary-diagenetic ore fabrics in the strata- and time-bound scheelite deposits of Kleinarl and Felbertal in the Eastern Alps. *Miner Deposita* 7:217–226. <https://doi.org/10.1007/BF00207156>
- Horstwood MSA, Košler J, Gehrels G, Jackson SE, McLean NM, Paton C, Pearson NJ, Sircombe K, Sylvester PJ, Vermeesch P, Bowring JF, Condon DJ, Schoene B (2016) Community-derived standards for LA-ICP-MS U-(Th)-Pb geochronology – uncertainty propagation, age interpretation and data reporting. *Geostand Geoanal Res* 40:311–332. <https://doi.org/10.1111/j.1751-908X.2016.00379.x>
- Iglseder C (2019) Geologische und Tektonische Karte der Gurktaler Alpen 1:250.000. In: Griesmeier GEU, Iglseder C (eds) *Arbeitstagung 2019 der Geologischen Bundesanstalt: Geologie des Kartenblattes GK25 Radenthein-Ost*: Murau 24–27 Juni 2019. Verlag der Geologischen Bundesanstalt, Wien, pp 48–54
- Iglseder C, Huet B (2019) Tektonische Einheiten auf GK25 Blatt Radenthein-Ost und angrenzenden Gebieten. In: Griesmeier GEU, Iglseder C (eds) *Arbeitstagung 2019 der Geologischen Bundesanstalt: Geologie des Kartenblattes GK25 Radenthein-Ost*: Murau 24–27 Juni 2019. Verlag der Geologischen Bundesanstalt, Wien, pp 5–18
- Iglseder C, Huet B, Rantitsch G, Ratschbacher L, Pfänder J (2016) Age and structure of the Stolzalpe Nappe - Evidence for Variscan metamorphism, Eoalpine top-to-the-WNW thrusting and top-to-the-ESE normal faulting (Gurktal Alps, Austria). In: Ortner H (ed) *Abstract Volume of GeoTirol2016 - Annual Meeting of DGGV and PANGEO Austria*, 25–28 September 2016, Innsbruck. Universität Innsbruck, Austria, p 137
- Iglseder C, Van Husen D, Huet B, Knoll T, Schönlaub HP (2019) Geologische Karte der Republik Österreich 1:25.000, Blatt Radenthein - Nordost. Verlag der Geologischen Bundesanstalt, Wien
- Jackson SE, Pearson NJ, Griffin WL, Belousova EA (2004) The application of laser ablation-inductively coupled plasma-mass spectrometry to in situ U-Pb zircon geochronology. *Chem Geol* 211:47–69. <https://doi.org/10.1016/j.chemgeo.2004.06.017>
- Jochum KP, Willbold M, Raczek I, Stoll B, Herwig K (2005) Chemical characterisation of the USGS reference glasses GSA-1G, GSC-1G, GSD-1G, GSE-1G, BCR-2G, BHVO-2G and BIR-1G using EPMA, ID-TIMS, ID-ICP-MS and LA-ICP-MS. *Geostand Geoanal Res* 29:285–302. <https://doi.org/10.1111/j.1751-908X.2005.tb00901.x>
- Jochum KP, Weis U, Stoll B, Kuzmin D, Yang Q, Raczek I, Jacob DE, Stracke A, Birbaum K, Frick DA, Günther D, Enzweiler J (2011) Determination of reference values for NIST SRM 610–617 glasses following ISO guidelines. *Geostand Geoanal Res* 35:397–429. <https://doi.org/10.1111/j.1751-908X.2011.00120.x>
- Kelly SD, Newville MG, Cheng L, Kemner KM, Sutton SR, Fenter P, Sturchio NC, Spötl C (2003) Uranyl incorporation in natural calcite. *Environ Sci Tech* 37:1284–1287. <https://doi.org/10.1021/es025962f>
- Knoll T, Huet B, Schuster R, Mali H, Ntaflou T, Hauzenberger C (2023) Lithium pegmatite of anatectic origin - a case study from the Austroalpine Unit Pegmatite Province (Eastern European Alps): geological data and geochemical model. *Ore Geol Rev* 105298. <https://doi.org/10.1016/j.oregeorev.2023.105298>
- Kozlik M, Raith JG (2017) Variscan metagranitoids in the central Tauern Window (Eastern Alps, Austria) and their role in the formation of the Felbertal scheelite deposit. *Lithos* 278–281:303–320. <https://doi.org/10.1016/j.lithos.2017.02.003>
- Kozlik M, Gerdes A, Raith JG (2016) Strontium isotope systematics of scheelite and apatite from the Felbertal tungsten deposit, Austria – results of in-situ LA-MC-ICP-MS analysis. *Miner Petrol* 110:11–27. <https://doi.org/10.1007/s00710-015-0416-0>
- Kozur HW (1991) The evolution of the Meliata-Hallstatt ocean and its significance for the early evolution of the Eastern Alps and Western Carpathians. *Palaeogeogr Palaeoclimatol* 87:109–135. [https://doi.org/10.1016/0031-0182\(91\)90132-B](https://doi.org/10.1016/0031-0182(91)90132-B)
- Kralik M, Aharon P, Schroll E, Zachmann D (1989) Carbon and oxygen isotope systematics of magnesites: a review. In: Möller P (ed) *Magnesite - Geology, Mineralogy, Geochemistry, Formation of Mg-Carbonates*. Gebrüder Borntraeger, Berlin, pp 197–223
- Kroner U, Romer RL (2013) Two plates — many subduction zones: the Variscan orogeny reconsidered. *Gondwana Res* 24:298–329. <https://doi.org/10.1016/j.gr.2013.03.001>
- Kwak TAP, Tan TH (1981) The geochemistry of zoning in skarn minerals at the King Island (Dolphin) Mine. *Econ Geol Bull Soc* 76:468–497. <https://doi.org/10.2113/gsecongeo.76.2.468>
- Launay G, Sizaret S, Lach P, Melleton J, Gloaguen É, Poujol M (2021) Genetic relationship between greisenization and Sn-W mineralizations in vein and greisen deposits: insights from the Panasqueira deposit (Portugal). *Bull Soc Géol Fr* 192:2. <https://doi.org/10.1051/bsgf/2020046>
- Lecumberri-Sanchez P, Vieira R, Heinrich CA, Pinto F, Wälle M (2017) Fluid-rock interaction is decisive for the formation of tungsten deposits. *Geology* 45:579–582. <https://doi.org/10.1130/G38974.1>
- Leitner C, Neubauer F, Marschallinger R, Genser J, Bernroider M (2013) Origin of deformed halite hopper crystals, pseudomorph anhydrite cubes and polyhalite in Alpine evaporites (Austria,

- Germany). *Int J Earth Sci* 102:813–829. <https://doi.org/10.1007/s00531-012-0836-6>
- Li W-S, Ni P, Pan J-Y, De Vivo B, Albanese S, Fan M-S, Gao Y, Zhang D-X, Chi Z (2022) Co-genetic formation of scheelite- and wolframite-bearing quartz veins in the Chuankou W deposit, South China: evidence from individual fluid inclusion and wall-rock alteration analysis. *Ore Geol Rev* 142:104723. <https://doi.org/10.1016/j.oregeorev.2022.104723>
- Linnen RL, Williams-Jones AE (1995) Genesis of a magmatic metamorphic hydrothermal system; the Sn-W polymetallic deposits at Pilok, Thailand. *Econ Geol* 90:1148–1166. <https://doi.org/10.2113/gsecongeo.90.5.1148>
- Liu X, Xiao C, Wang Y (2021) The relative solubilities of wolframite and scheelite in hydrothermal fluids: Insights from thermodynamic modeling. *Chem Geol* 584:120488. <https://doi.org/10.1016/j.chemgeo.2021.120488>
- Lüders V, Romer R, Gilg HA, Bodnar RJ, Pettke T, Misantoni D (2009) A geochemical study of the Sweet Home Mine, Colorado Mineral Belt, USA: hydrothermal fluid evolution above a hypothesized granite cupola. *Miner Deposita* 44:415–434. <https://doi.org/10.1007/s00126-008-0221-3>
- Ludwig KR (1998) On the treatment of concordant uranium-lead ages. *Geochim Cosmochim Acta* 62:665–676. [https://doi.org/10.1016/S0016-7037\(98\)00059-3](https://doi.org/10.1016/S0016-7037(98)00059-3)
- Lünsdorf NK, Dunkl I, Schmidt BC, Rantitsch G, von Eynatten H (2017) Towards a higher comparability of geothermometric data obtained by Raman spectroscopy of carbonaceous material. Part 2: A Revised Geothermometer. *Geostand Geoanal Res* 41:593–612. <https://doi.org/10.1111/ggr.12178>
- Macavei J, Schulz H (1993) The crystal structure of wolframite type tungstates at high pressure. *Z Krist-Cryst Mater* 207:193–208. <https://doi.org/10.1524/zkri.1993.207.Part-2.193>
- Maucher A (1965) Die Antimon-Wolfram-Quecksilber Formation und ihre Beziehungen zu Magmatismus und Geotektonik. *Freiberg Forsch HC* 186:173–187
- McDonough WF, Sun SS (1995) The composition of the Earth. *Chem Geol* 120:223–253. [https://doi.org/10.1016/0009-2541\(94\)00140-4](https://doi.org/10.1016/0009-2541(94)00140-4)
- Michaud JA-S, Gumiaux C, Pichavant M, Gloaguen E, Marcoux E (2020) From magmatic to hydrothermal Sn-Li-(Nb-Ta-W) mineralization: the Argemela area (central Portugal). *Ore Geol Rev* 116:103215. <https://doi.org/10.1016/j.oregeorev.2019.103215>
- Miranda ACR, Beaudoin G, Rottier B (2022) Scheelite chemistry from skarn systems: implications for ore-forming processes and mineral exploration. *Miner Deposita*. <https://doi.org/10.1007/s00126-022-01118-y>
- Nassau K, Loiacono GM (1963) Calcium tungstate—III: trivalent rare earth substitution. *J Phys Chem Solids* 24:1503–1510. [https://doi.org/10.1016/0022-3697\(63\)90090-8](https://doi.org/10.1016/0022-3697(63)90090-8)
- Neinavaie H (1984) Wolframvorkommen in der Gurktaler Quarzphylitzone im Nockgebiet/Kärnten. *Anz Österr Akad Wiss, Math-Nat Kl* 121:135
- Neinavaie H, Thalmann F, Ataii B, Beran A (1989) Wolframite- and scheelite-bearing carbonate rocks of the Nock Mountains, Austria; a new type of tungsten mineralization in the Eastern Alps. *Miner Deposita* 24:14–18. <https://doi.org/10.1007/BF00206716>
- Neubauer F, Genser J, Handler R (2000) The Eastern Alps: result of a two-stage collision process. *Mitt Österr Geol G* 92:117–134
- Neubauer F, Genser J, Bernroider M, Stauber O, Yuan S, Liu X, Dong Y, Cao S (2019) The Gurktal Nappe Complex and its frame. In: Griesmeier GEU, Iglseider C (eds) *Arbeitstagung 2019 der Geologischen Bundesanstalt: Geologie des Kartenblattes GK25 Radenthein-Ost: Murau 24–27 Juni 2019*. Verlag der Geologischen Bundesanstalt, Wien, pp 133–152
- Neubauer F, Liu Y, Dong Y, Chang R, Genser J, Yuan S (2022) Pre-Alpine tectonic evolution of the Eastern Alps: from Prototethys to Paleotethys. *Earth-Sci Rev* 226:103923. <https://doi.org/10.1016/j.earscirev.2022.103923>
- Palmer MC, Scanlan EJ, Scott JM, Farmer L, Pickering D, Wilson VJ, Oelze M, Craw D, le Roux PJ, Luo Y, Graham Pearson D, Reid MR, Stirling CH (2022) Distinct scheelite REE geochemistry and ⁸⁷Sr/⁸⁶Sr isotopes in proximally- and distally-sourced metamorphogenic hydrothermal systems, Otago Schist. *New Zealand Ore Geol Rev* 144:104800. <https://doi.org/10.1016/j.oregeorev.2022.104800>
- Paton C, Hellstrom J, Paul B, Woodhead J, Hergt J (2011) Iolite: Freeware for the visualisation and processing of mass spectrometric data. *J Anal at Spectrom* 26:2508–2518. <https://doi.org/10.1039/C1JA10172B>
- Pistotnik J (1996) *Geologische Karte der Republik Österreich 1:50.000, ÖK 183, Bl. Radenthein*. Verlag der Geologischen Bundesanstalt (GBA), Wien
- Pohl W (1990) Genesis of magnesite deposits — models and trends. *Geol Rundsch* 79:291–299. <https://doi.org/10.1007/BF01830626>
- Poitrenaud T, Poujol M, Augier R, Marcoux E (2020) The poly-phase evolution of a late Variscan W/Au deposit (Salau, French Pyrenees): insights from REE and U/Pb LA-ICP-MS analyses. *Miner Deposita* 55:1127–1147. <https://doi.org/10.1007/s00126-019-00923-2>
- Poulin RS, McDonald AM, Kontak DJ, McClenaghan MB (2016) On the relationship between cathodoluminescence and the chemical composition of scheelite from geologically diverse ore-deposit environments. *Can Min* 54:1147–1173. <https://doi.org/10.3749/canmin.1500023>
- Poulin RS, Kontak DJ, McDonald A, McClenaghan MB (2018) Assessing scheelite as an ore-deposit discriminator using its trace-element and REE chemistry. *Can Min* 56:265–302. <https://doi.org/10.3749/canmin.1800005>
- Prochaska W (1997) Die Bedeutung der chemischen Zusammensetzung von Einschlußfluiden und laugbaren Salzen für die Genese von hydrothermalen und sedimentären Karbonatgesteinen der Ostalpen. *Austrian J Earth Sci* 90:175–183
- Prochaska W (2016) Genetic concepts on the formation of the Austrian magnesite and siderite mineralizations in the Eastern Alps of Austria. *Geol Croat* 69:31–38. <https://doi.org/10.4154/GC.2016.03>
- Prochaska W, Henjes-Kunst F (2009) Genese der Sideritvererzungen der Östlichen Grauwackenzone - aktueller Stand der Forschung. In: Bryda G, Seifert P (eds) *Arbeitstagung 2009 der Geologischen Bundesanstalt Blatt 101 Eisenerz: Leoben*. Verlag der Geologischen Bundesanstalt, Wien, pp 153–169
- Putnis A (2002) Mineral replacement reactions: from macroscopic observations to microscopic mechanisms. *Mineral Mag* 66:689–708. <https://doi.org/10.1180/0026461026650056>
- Raith JG (1991) Stratabound tungsten mineralization in regional metamorphic calc-silicate rocks from the Austroalpine Crystalline Complex, Austria. *Miner Deposita* 26:72–80. <https://doi.org/10.1007/BF00202370>

- Raith JG, Stein HJ (2006) Variscan ore formation and metamorphism at the Felbertal scheelite deposit (Austria): constraining tungsten mineralisation from Re–Os dating of molybdenite. *Contrib Mineral Petr* 152:505–521. <https://doi.org/10.1007/s00410-006-0118-z>
- Raith JG, Papesch W, Schroll E (1988) Kohlenstoff- und Sauerstoffisotope scheelitfreier und scheelitführender Karbonatgesteine aus den Ostalpen. *Anz Österr Akad Wiss, Math-Nat Kl* 125. Jahrgang 1988:59–64
- Raith JG, Grum W, Prochaska W, Frank W (1995) Polymetamorphism and polyphase deformation of the strata-bound magnesite-scheelite deposit, Tux-Lanersbach, Eastern Alps, Austria. *Econ Geol* 90:763–781. <https://doi.org/10.2113/gsecongeo.90.4.763>
- Raith JG, Schmidt S, Aupers K (2018) Field trip pre-EX-5. Tungsten deposit Felbertal, Salzburg, Austria. In: Neubauer F (ed) XXI International Congress of the Carpathian Balkan Geological Association: Guidebook to pre- and post-conference excursions: Salzburg, September 10–13, 2018. Geological Survey of Austria, Vienna, pp 7–46
- Rantitsch G, Rußegger B (2000) Thrust-related very low grade metamorphism within the Gurktal Nappe Complex (Eastern Alps). *Jb Geol B-A* 142:219–225
- Rantitsch G, Iglseider C, Schuster R, Hollinetz MS, Huet B, Werdenich M (2020) Organic metamorphism as a key for reconstructing tectonic processes: a case study from the Austroalpine unit (Eastern Alps). *Int J Earth Sci* 109:2235–2253. <https://doi.org/10.1007/s00531-020-01897-7>
- Romer RL, Kroner U (2016) Phanerozoic tin and tungsten mineralization—tectonic controls on the distribution of enriched protoliths and heat sources for crustal melting. *Gondwana Res* 31:60–95. <https://doi.org/10.1016/j.gr.2015.11.002>
- Roy-Garand A, Adlakha E, Hanley J, Elongo V, Lecumberri-Sanchez P, Falck H, Boucher B (2022) Timing and sources of skarn mineralization in the Canadian Tungsten Belt: revisiting the paragenesis, crystal chemistry and geochronology of apatite. *Miner Deposita* 57:1391–1413. <https://doi.org/10.1007/s00126-022-01107-1>
- Schmid SM, Fügenschuh B, Kissling E, Schuster R (2004) Tectonic map and overall architecture of the Alpine orogen. *Eclogae Geol Helv* 97:93–117. <https://doi.org/10.1007/s00015-004-1113-x>
- Schuster R, Stüwe K (2008) Permian metamorphic event in the Alps. *Geology* 36:603–606. <https://doi.org/10.1130/G24703A.1>
- Sciuba M, Beaudoïn G, Grzela D, Makvandi S (2020) Trace element composition of scheelite in orogenic gold deposits. *Miner Deposita* 55:1149–1172. <https://doi.org/10.1007/s00126-019-00913-4>
- Shannon R (1976) Revised effective ionic radii and systematic study of inter atomic distances in halides and chalcogenides. *Acta Crystallogr A* 32:751–767. <https://doi.org/10.1107/s0567739476001551>
- Shore M, Fowler AD (1996) Oscillatory zoning in minerals; a common phenomenon. *Can Mineral* 34:1111–1126
- Simons B, Andersen JCØ, Shail RK, Jenner FE (2017) Fractionation of Li, Be, Ga, Nb, Ta, In, Sn, Sb, W and Bi in the peraluminous Early Permian Variscan granites of the Cornubian Batholith: precursor processes to magmatic-hydrothermal mineralisation. *Lithos* 278–281:491–512. <https://doi.org/10.1016/j.lithos.2017.02.007>
- Sláma J, Košler J, Condon DJ, Crowley JL, Gerdes A, Hanchar JM, Horstwood MSA, Morris GA, Nasdala L, Norberg N, Schaltegger U, Schoene B, Tubrett MN, Whitehouse MJ (2008) Plešovice zircon — a new natural reference material for U–Pb and Hf isotopic microanalysis. *Chem Geol* 249:1–35. <https://doi.org/10.1016/j.chemgeo.2007.11.005>
- Staude S, Bons PD, Markl G (2009) Hydrothermal vein formation by extension-driven dewatering of the middle crust: an example from SW Germany. *Earth Planet Sc Lett* 286:387–395. <https://doi.org/10.1016/j.epsl.2009.07.012>
- Su S-Q, Qin K-Z, Li G-M, Olin P, Thompson J (2019) Cathodoluminescence and trace elements of scheelite: constraints on ore-forming processes of the Dabaoshan porphyry Mo–W deposit. *South China Ore Geol Rev* 115:103183. <https://doi.org/10.1016/j.oregeorev.2019.103183>
- Swart PK, Moore F (1982) The occurrence of uranium in association with cassiterite, wolframite, and sulphide mineralization in South-West England. *Mineral Mag* 46:211–215. <https://doi.org/10.1180/minmag.1982.046.339.07>
- Sylvester H (1989) Vergleich von Perm/Skyth-Profilen des Ober-, Mittel- und Unterostalpins. *Jb Geol B-A* 132:791–821
- Tanis EA, Simon A, Tschauer O, Chow P, Xiao Y, Burnley P, Cline CJ, Hanchar JM, Pettke T, Shen G, Zhao Y (2015) The mobility of Nb in rutile-saturated NaCl- and NaF-bearing aqueous fluids from 1–6.5 GPa and 300–800 °C. *Am Mineral* 100:1600–1609. <https://doi.org/10.2138/am-2015-5031>
- Thalmann F, Ronge W (1987) Geowissenschaftliche und bergtechnische Untersuchung der Scheelit-Wolframitmineralisation im Gebiet Mallnock (Kärnten) 1981–1987. Abschlussbericht. VOEST-ALPINE AG, Eisenerz
- Thalmann F, Schermann O, Cerny I, Meyer J, Malecki G, Ronge W, Schroll E (1987) Geochemischer Atlas der Republik Österreich 1:1.000.000: Böhmisches Masse und Zentralzone der Ostalpen: Bachsedimente Fraktion <0,18 mm (<80 mesh). Element: Wolfram. Verlag der Geologischen Bundesanstalt, Wien
- Tindle AG, Webb PC (1989) Niobium wolframite from Glen Gairn in the Eastern Highlands of Scotland: a microprobe investigation. *Geochim Cosmochim Acta* 53:1921–1935. [https://doi.org/10.1016/0016-7037\(89\)90313-X](https://doi.org/10.1016/0016-7037(89)90313-X)
- Vermeech P (2018) IsoplotR: a free and open toolbox for geochronology. *Geosci Front* 9:1479–1493. <https://doi.org/10.1016/j.gsf.2018.04.001>
- Wang X, Qiu Y, Lu J, Chou IM, Zhang W, Li G, Hu W, Li Z, Zhong R (2020) In situ Raman spectroscopic investigation of the hydrothermal speciation of tungsten: Implications for the ore-forming process. *Chem Geol* 532:119299. <https://doi.org/10.1016/j.chemgeo.2019.119299>
- Wang M, Zhao R, Shang X, Wei K, Liu K, An W (2022) REE and cathodoluminescence features of scheelites from the Tongshankou Cu–Mo deposit in Eastern China. *Ore Geol Rev* 147:104998. <https://doi.org/10.1016/j.oregeorev.2022.104998>
- Webster J, Thomas R, Förster H-J, Seltmann R, Tappen C (2004) Geochemical evolution of halogen-enriched granite magmas and mineralizing fluids of the Zinnwald tin-tungsten mining district, Erzgebirge, Germany. *Miner Deposita* 39:452–472. <https://doi.org/10.1007/s00126-004-0423-2>
- Wenger H (1964) Die Scheelitlagerstätte. *Tux Radex Rundsch* 1964:109–132
- Wiedenbeck M, Allé P, Corfu F, Griffin WL, Meier M, Oberli F, Quadt AV, Roddick JC, Spiegel W (1995) Three natural zircon standards for U–Th–Pb, Lu–Hf, trace element and REE analyses. *Geostand Newsl* 19:1–23. <https://doi.org/10.1111/j.1751-908X.1995.tb00147.x>

- Wintzer NE (2019) Geology, geochronology, and geochemistry of the stibnite-Yellow Pine gold-antimony-tungsten mining area, Idaho. Dissertation, Washington State University
- Wintzer NE, Schmitz MD, Gillerman VS, Vervoort JD (2020) Isotopic ratios and element concentrations of U-Pb and Sm-Nd for scheelite petrochronology. U.S. Geological Survey Data Release. <https://doi.org/10.5066/P9QH5ZYP>
- Wintzer NE, Schmitz MD, Gillerman VS, Vervoort JD (2022) U-Pb scheelite ages of tungsten and antimony mineralization in the Stibnite-Yellow Pine District, Central Idaho. *Econ Geol.* <https://doi.org/10.5382/econgeo.4953>
- Wood SA, Samson IM (2000) The hydrothermal geochemistry of tungsten in granitoid environments: I. Relative solubilities of ferberite and scheelite as a function of T, P, pH, and mNaCl. *Econ Geol* 95:143–182. <https://doi.org/10.2113/gsecongeo.95.1.143>
- Xie W, Zeng Q, Zhou L, Lan T, Wang R, Wu J (2022) Ore genesis of the Baishitouwa Quartz-Wolframite vein-type deposit in the Southern Great Xing'an Range W Belt, NE China: constraints from wolframite in-situ geochronology and geochemistry analyses. *Minerals* 12:515. <https://doi.org/10.3390/min12050515>
- Yang M, Yang Y, Wu S, Romer R, Che X, Zhao Z-F, Li W, Yang J-H, Wu F-Y, Xie L, Huang C, Zhang D, Zhang Y (2020) Accurate and precise in situ U-Pb isotope dating of wolframite series minerals via LA-SF-ICP-MS. *J Anal At Spectrom* 35:2191–2203. <https://doi.org/10.1039/D0JA00248H>
- Zanetti A, Mazzucchelli M, Sinigoi S, Giovanardi T, Peressini G, Fanning M (2013) SHRIMP U-Pb zircon triassic intrusion age of the finero mafic complex (Ivrea-Verbano Zone, Western Alps) and its geodynamic implications. *J Petrol* 54:2235–2265. <https://doi.org/10.1093/petrology/egt046>
- Zhang Q, Zhang R-Q, Gao J-F, Lu J-J, Wu J-W (2018) In-situ LA-ICP-MS trace element analyses of scheelite and wolframite: constraints on the genesis of veinlet-disseminated and vein-type tungsten deposits, South China. *Ore Geol Rev* 99:166–179. <https://doi.org/10.1016/j.oregeorev.2018.06.004>
- Zhao WW, Zhou M-F, Williams-Jones AE, Zhao Z (2018) Constraints on the uptake of REE by scheelite in the Baoshan tungsten skarn deposit, South China. *Chem Geol* 477:123–136. <https://doi.org/10.1016/j.chemgeo.2017.12.020>

Publisher's Note Springer Nature remains neutral with regard to jurisdictional claims in published maps and institutional affiliations.